Thermo-electrochemical Model of a Zinc-air Flow Battery

by

Stephen Alan Murphy
B.Eng., University of Victoria, 2015

Submitted in Partial Fulfillment of the
Requirements for the Degree of

MASTER OF ENGINEERING

in the Department of Mechanical Engineering

We acknowledge with respect the Lekwungen peoples on whose traditional territory the university stands and the Songhees, Esquimalt and W̱SÁNEĆ peoples whose historical relationships with the land continue to this day.

Thermo-electrochemical Model of a Zinc-air Flow Battery

by

Stephen Alan Murphy
B.Eng., University of Victoria, 2015

Supervisory Committee

Dr. Andrew Rowe (Dept. of Mechanical Engineering)

Supervisor

Dr. Curran Crawford (Dept. of Mechanical Engineering)

Departmental Member

ABSTRACT

As renewable energy production has become more popular in society, the need for large scale energy storage has increased. By storing energy from sources such as solar and wind power, energy can be produced when it is most feasible and dispatched when there is demand. Such infrastructure would significantly increase the viability of renewable energy technologies. Zinc-air batteries are a promising type of energy storage system which has the potential to solve the grid energy storage problem. A thermo-electrochemical model was developed to provide an order-of-magnitude approximation of the performance of a novel zinc-air battery which has separate charge and discharge stacks coupled with a large fuel storage reservoir. This configuration enables independent scaling of system discharge output power, charge speed, and energy capacity. Because of this flexibility, the system could be tailored to various projects as needed where there may be more importance on some performance characteristics over others. The model was validated using a reference case where the results were evaluated. The capabilities of the model were discussed, including the advantages and disadvantages. The model performs well for order-of-magnitude level approximations of system performance, and opportunities to refine the model in the future were suggested.

TABLE OF CONTENTS

LIST OF FIGURES

LIST OF TABLES

ACKNOWLEDGEMENT

This work would not have been possible without the kindness and support of my supervisor, Dr. Andrew Rowe. Dr. Rowe was a fantastic mentor and problem solver throughout my master's. His support and enthusiasm over the program made working together a pleasure.

Secondly, I would like to give my sincere thanks to Laura Magallanes Ibarra, who donated much of her time to helping me develop this model. Laura's expertise and positivity made a large impact on my work and I wish her good luck in her own master's defence and future endeavours.

Thirdly, I would like to thank my friends and family who motivated me to do my master's and encouraged me all the while.

Last, but not least, I would like to thank the University of Victoria, with notable mention of Jaerang Lee, who was always a phone call away to help guide me through the program successfully.

1 INTRODUCTION

This report outlines the work that was performed in the development of a thermo-electrochemical model of a novel zinc-air flow battery. The report will first discuss the motivation behind zinc-air battery research. Then, the typical characteristics and operation of zinc-air batteries will be discussed. Following that, a newly developed model will be detailed, and the performance of the model will be evaluated.

1.1 BACKGROUND

As renewable energy technologies become more prevalent in society, many new challenges are being identified. The variability of energy production from wind or solar powered devices is a large hurdle in the journey to large scale adoption of these technologies. For example, solar panels convert the sun's radiation into electricity most effectively at solar noon, when the sun is shining directly on the panel. However, at night there is no solar radiation incident on solar panels and therefore no energy is produced. Even at times closer to sunrise and sunset, when the sun is low in the sky, the energy production is greatly diminished. Similarly, variation in wind speed causes the energy production of wind turbine farms to be very inconsistent. These variations in wind speed can be caused by season, geographical location, large- and small-scale weather patterns, and many other factors.

Like the supply of renewable energy, the demand for energy is also variable. Demand for electricity can vary based on many factors such as the time of year, how much heating or air conditioning people use in their homes, and whether people are at home or in the office, to name a few. Naturally, the supply and demand cycles of energy production are never fully in unison, and this is especially true now that many sources of energy are weather dependent rather than coal or nuclear power which can be operated as needed. To alleviate this problem, there is now a clear need for large-scale energy storage so that energy can be produced and used at different times.

Many possible solutions to the energy storage challenge have been investigated [1]. Although there are several kinds of energy storage, the most popular area of research is in chemical storage, including batteries and fuel cells. For example, lithium-based batteries have relatively good power density and have been used extensively in phones and vehicles. However, lithium-based batteries such as lithium-ion are often too expensive for large scale grid energy storage [2].

A promising new area of battery technology is metal-air batteries [3]. Metal-air batteries are advantageous in that oxygen from the air is used for the cathode of the battery, which means that the cathodic species does not need to be contained within the battery packaging and therefore the energy density is greatly increased [4]. One type of metal-air batteries about which researchers are very hopeful is the zinc-air battery. Zinc-air batteries are advantageous over other metal-air batteries because their primary anodic material is zinc, which is the 4th most abundant element in the earth's crust and is widely available for low cost. Additionally, zinc-air batteries are inherently non-flammable which means that they are far safer than technologies such as Lithium-ion or Lithium-air batteries [1]. Zinc-air batteries have also been vetted through their widespread use in hearing aids, which further increases confidence in their technological viability.

1.2 MOTIVATION

Given the growing need for large-scale energy storage and the significant research and development effort required to implement such a new capability, there is still more room for improvement to achieve both technical and commercial success. The academic community, and several industrial partners, are working to improve zinc-air battery technology in the pursuit of solving our energy storage needs. Most research that has been done today has been on prototype or lab quality setups rather than full-scale systems. Therefore, the work outlined in this report is intended to support the academic and industrial communities in better understanding zinc-air systems at a system level.

1.3 OBJECTIVE

The objective of this work was to develop a thermo-electrochemical model for a novel configuration of a secondary zinc-air battery that has not been investigated significantly in the academic community. By developing a model of a real-world configuration, the performance of an actual zinc-air system can be evaluated. The intention with this work is to provide a simplified model as a first step, which can then be later upgraded to become more sophisticated. As there are extremely few zinc-air batteries that have been deployed to date, this model will serve as a tool to help designers create new battery designs.

This chapter introduced the topic that was researched and the model that was developed. The grid energy storage problem is a major hurdle in the adoption of renewable technologies, though there is significant research going on into many areas to solve this problem. Zinc-air batteries are a promising candidate for this application. Chapter 2 will introduce zinc-air flow batteries in more detail.

2 ZINC-AIR FLOW BATTERIES

This chapter will describe characteristics of zinc-air batteries in general.

2.1 OVERVIEW

Zinc-air batteries operate by creating a redox (reduction-oxidation) reaction with zinc metal as the anodic material and oxygen gas from air as the cathodic material. At the cathode, the following reduction half-reaction proceeds as follows [5]:

$$\frac{1}{2}O_2 + H_2O + 2e^- \rightarrow 2OH^-,\ E^0 = 0.401\ V \tag{2.1}$$

and at the zinc anode, the oxidation half-reaction [5] is given as:

$$Zn + 4OH^- \rightarrow Zn(OH)_4^{2-} + 2e^-,\ E^0 = -1.199\ V \tag{2.2}$$

As zinc and hydroxyl ions react to form zincate ions ($Zn(OH)_4^{2-}$), eventually zincate reaches a saturation limit where it then further oxidizes to zinc oxide, which is the reaction found in most literature [5]. However, in this case zincate will be considered the final product and it will be assumed that the zincate saturation limit is never reached. Therefore, the overall reaction is as follows:

$$\frac{1}{2}O_2 + 2OH^- + H_2O + Zn \rightarrow Zn(OH)_4^{2-},\ E^0 = 1.600\ V \tag{2.3}$$

The anode and cathode are typically separated by an electrolyte, which in this case is potassium hydroxide [6]. As shown, electrons are released at the anode which are then collected by a current collector and delivered to a load. The electrons then continue along the circuit back to the cathode where they react with oxygen and water to create hydroxyl ions.

An example primary zinc-air battery can be seen below in Figure 2.1. Primary batteries are batteries which cannot be recharged once depleted, whereas secondary batteries are batteries which can be recharged once depleted [4]. Zinc-air batteries throughout research typically have slurry-type electrolytes, where the anodic species (in this case zinc) is distributed throughout an electrolyte (most often potassium hydroxide) in particulate form [3]. On the cathode side, an air electrode facilitates intake of oxygen gas from the air. Between the zinc-electrolyte slurry and the air electrode is a separator which is responsible for allowing oxygen to pass into the slurry while preventing evaporation of water or diffusion of particles in the slurry out of the cell. On both the anode and cathode ends of the cell, current collectors transfer electrons in and out of the cell as the reaction proceeds [4].

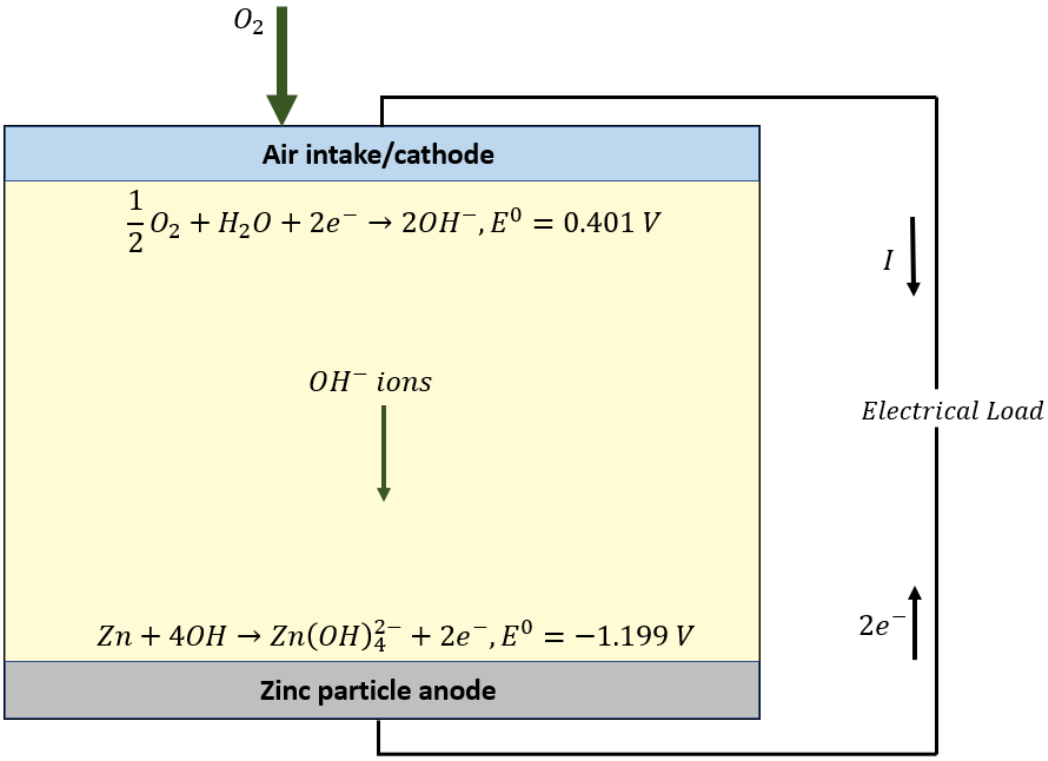

Figure 2.1: Simplified representation of a zinc-air battery cell

2.2 AREAS OF RESEARCH

The type of zinc-air battery being investigated for large-scale grid energy storage differs from that of the zinc-air battery used for hearing aids. Firstly, primary batteries are used for hearing aids [4]. For full-scale grid energy storage, rechargeability is a key requirement. Therefore, much of the research going on today in zinc-air batteries is in developing secondary zinc-air batteries.

As research into reusability has progressed, a few issues have dominated during the development of secondary zinc-air batteries. Firstly, as zinc forms zincate (and zinc oxide in most literature), the zincate builds up on the anode of the cell which causes passivation of the anode [4]. Another issue is the formation of dendrites which can pierce separators and cause the cell to short circuit [4]. When recharging the cell, zinc may not necessarily be evolved at the same place where it oxidized to zincate or zinc oxide, which causes shape change of the anode [4]. For these and several other reasons, flow battery configurations have dominated research. A typical flow battery will consist of a flowing electrolyte which assists in transporting waste material (in this case zincate) away from the cell in order to minimize the problems described above. An example zinc-air flow battery can be seen below in Figure 2.2. As shown, a reservoir of zinc-electrolyte slurry material is included, which is often used to increase the capacity of the cell without increasing the cell and therefore the electrode size. This is advantageous because it allows independent scaling of cell capacity and power.

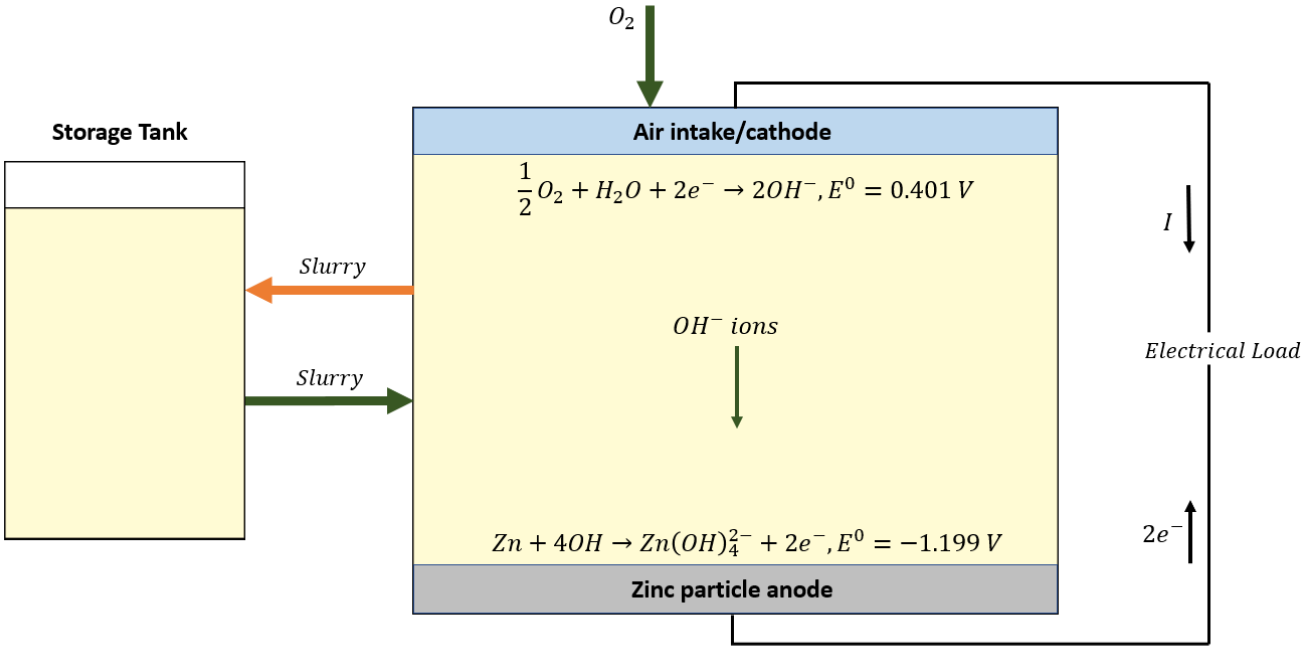

Figure 2.2: Simplified representation of a zinc-air flow battery cell with storage tank

2.3 TYPICAL BATTERY PERFORMANCE

Flow batteries, like other batteries, have discharge and charge curves as shown in Figure 2.3 [5].

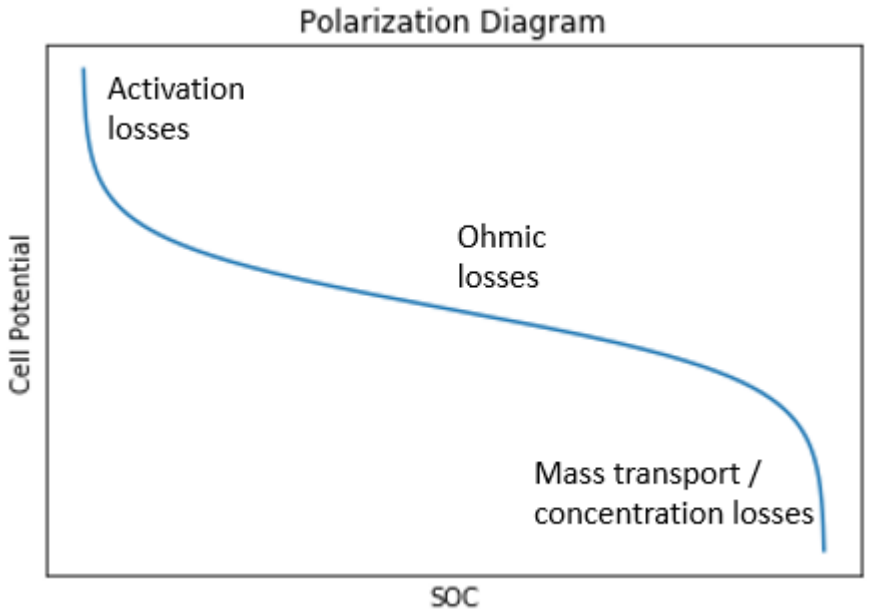

Figure 2.3: Typical cell polarization curve

The cell potential increases with increasing SOC (state of charge) and decreases with decreasing SOC. At low SOC, losses are primarily due to the activation overpotential of the cell. At high SOC, there are significant mass transport losses. In between these are primarily ohmic losses. These losses cause the cell potential to increase while charging and decrease while discharging. These losses also cause the efficiency of the cell to decrease, where efficiency is measured as the ratio of energy extracted from the cell while discharging to the energy delivered to the cell to charge it.

This chapter introduced zinc-air flow batteries and how they work. The overall reaction for the flow battery was described where the end-product was zincate. Chapter 3 will introduce the thermo-electrochemical model that was developed to simulate zinc-air flow battery systems.

3 THERMO-ELECTROCHEMICAL MODEL

This chapter will describe the model that was developed, including the configuration of the battery, the thermal components of the model, and the electrochemical components of the model.

3.1 CONFIGURATION

The configuration that was used for the model contains independent charging and discharging stacks connected via a storage tank as shown below in Figure 3.1. As shown, material is transported from one container to another, where oxygen is taken from the air into the discharge stack in order to proceed with the zinc-air redox reaction. In the charge stack, the redox reaction works in reverse which produces waste oxygen gas that is then exhausted to the atmosphere. Charging and discharging do not occur simultaneously, although material is circulated throughout all cells in order to maintain approximately equal concentrations everywhere.

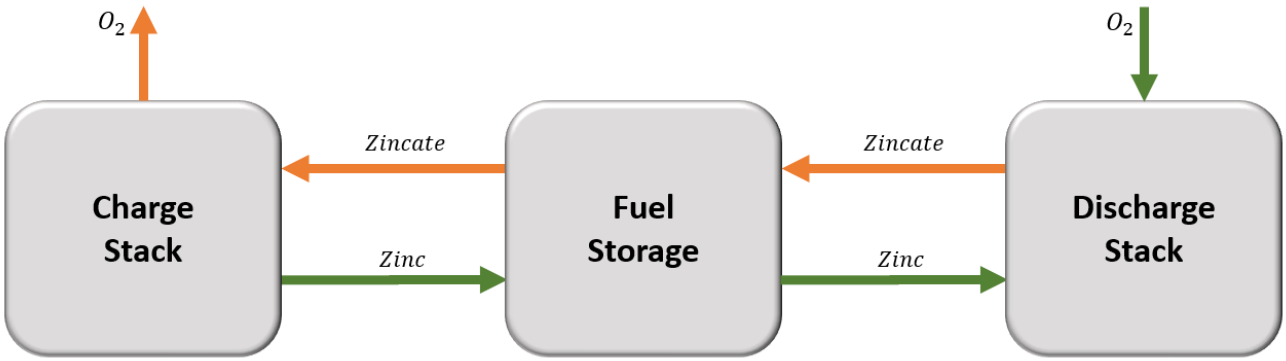

Figure 3.1: Simplified zinc-air battery configuration

This configuration is novel in that it deviates from the typical configuration where there would be one stack in which both charging and discharging would occur. By having separate stacks, the rate at which the system is discharged can be optimized separately from the rate at which the system is charged. By having each stack designed for a single purpose, higher efficiencies can be achieved by designing each cell for a single operating condition rather than two. With the addition of the separate fuel storage tank as in

other designs, the system is also capable of scaling the energy capacity independently from the discharge or charge power. This design is therefore extremely customizable for projects where there may be varying requirements, such as higher importance placed on fast charging, high capacity, etc.

3.2 MASS BALANCE

Assumptions for the mass transfer throughout the system include:

- Oxygen enters and exits the system only as is needed to participate in the chemical reaction. Therefore, there is never oxygen considered in the bulk electrolyte.
- Potassium hydroxide (electrolyte) is represented as hydroxyl ions and the potassium ions are ignored.
- Perfect, instantaneous mixing exists in each tank.
- A constant volume flow rate entering each of the stacks is assumed.

Starting with the discharge stack, a mixture of zinc, zincate, water, and potassium hydroxide enters the cell via the fuel storage tank and oxygen enters the cell from the air intake. The electrochemical reaction converts zinc, water, oxygen, and potassium hydroxide into zincate, which is then pumped out of the cell back to the fuel storage tank.

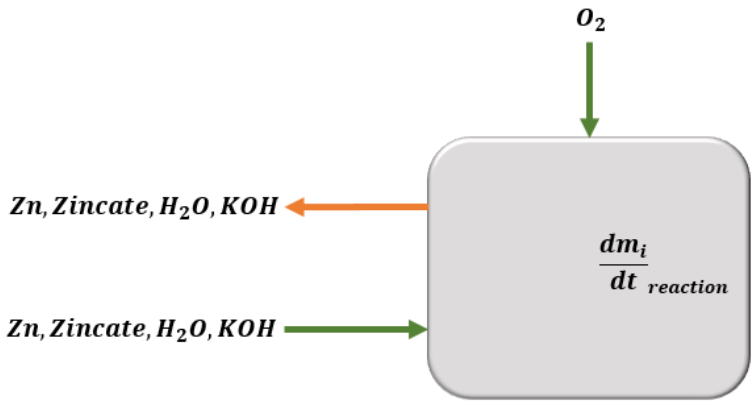

Figure 3.2: Discharge stack mass flows

The rate at which the products are created via the redox reaction is determined by Faraday's Law of Electrolysis, as shown in equation (3.1), where $\dot{n}_{reac}$ is the rate at which the products are created in mol/s, I is the cell current in amperes, n_e is the number of electrons transferred per reaction (in this case 2), and F is Faraday's constant, which is equal to $96485 \frac{C}{mol}$.

$$\dot{n}_{reac} = \frac{I}{n_e F} \tag{3.1}$$

The mass balance for the discharge stack can therefore be described as:

$$\frac{dm_i}{dt} = \sum_{in} \dot{m}_i - \sum_{out} \dot{m}_i + \left(\frac{dm_i}{dt}\right)_{reac} \tag{3.2}$$

where m_i is the mass of species i, $\dot{m}_{i,reac}$ is the mass equivalent of Faraday's Law of Electrolysis, and t is the timestep. This can be expressed in terms of molar flows as:

$$\frac{dn_i}{dt} = \sum_{in} \dot{n}_i - \sum_{out} \dot{n}_i + \left(\frac{dn_i}{dt}\right)_{reac} \tag{3.3}$$

The same procedure is followed for the charge stack, where the mass flows are shown in Figure 3.3.

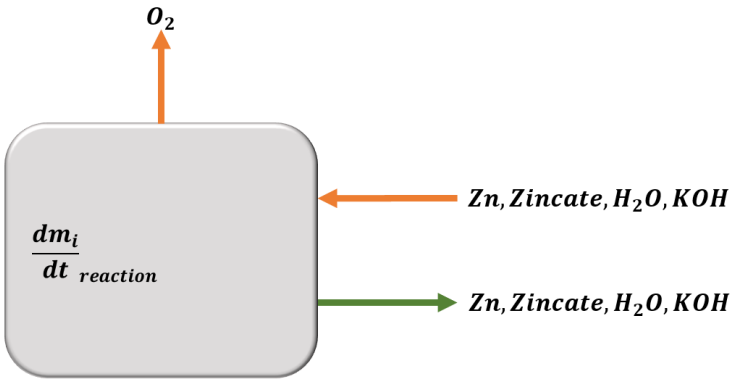

Figure 3.3: Charge stack mass flows

The fuel storage tank does not contain any electrochemical reactions, but it does contain mass flows to and from both the charge and discharge stacks as shown below in Figure 3.4.

Figure 3.4: Fuel storage tank mass flows

The mass balance equation is therefore:

$$\frac{dm_i}{dt} = \sum_{in} \dot{m}_i - \sum_{out} \dot{m}_i \tag{3.4}$$

which in terms of molar flows is expressed as:

$$\frac{dn_i}{dt} = \sum_{in} \dot{n}_i - \sum_{out} \dot{n}_i \tag{3.5}$$

In all containers, it is assumed that flow enters and exits each container at the same time as the reaction occurs for each time step. This implies that flow exiting each container will have concentrations equal to the concentrations of the bulk before the electrochemical reaction has occurred at each timestep. The effects of the electrochemical reaction will therefore affect concentrations of flows at each subsequent timestep, but not at the timestep at which the reaction occurs.

Given that material is transported in and out of the containers via pumps, a volume flow rate is defined for the material entering the system. The volume exiting each cell is then calculated such that mass of the discharge and charge cells is conserved. Due to the variation in densities of each species, this results in a corresponding volume and concentration change of both the discharge and charge tanks, which then

causes a subsequent change in volume and concentration of the storage tank. The mass conservation of the stacks is governed by:

$$\sum_{in} \dot{m}_{stack} - \sum_{out} \dot{m}_{stack} + \sum_{reac} \dot{m}_{stack} = 0 \tag{3.6}$$

which implies that as mass enters or exits the system (oxygen intake or exhaust), the total mass of the system will change.

3.3 THERMAL MODEL

Several assumptions were made in the development of the thermal model, including:

- Piping between containers are perfectly insulated (no heat gain or loss)
- Material is transferred from one container to another instantaneously
- No pumps are considered
- Conduction through container housings is ignored
- Heat loss through containers is assumed as natural convection with the air
- A housing for the complete system was not included and ambient temperature was assumed to be 298.15 K
- The intake oxygen was assumed to enter the system at 10 °C above ambient temperature (assumed air passes through scrubber to remove carbon dioxide which would slightly preheat the intake flow)

The heat flow of the discharge stack is shown below in Figure 3.5.

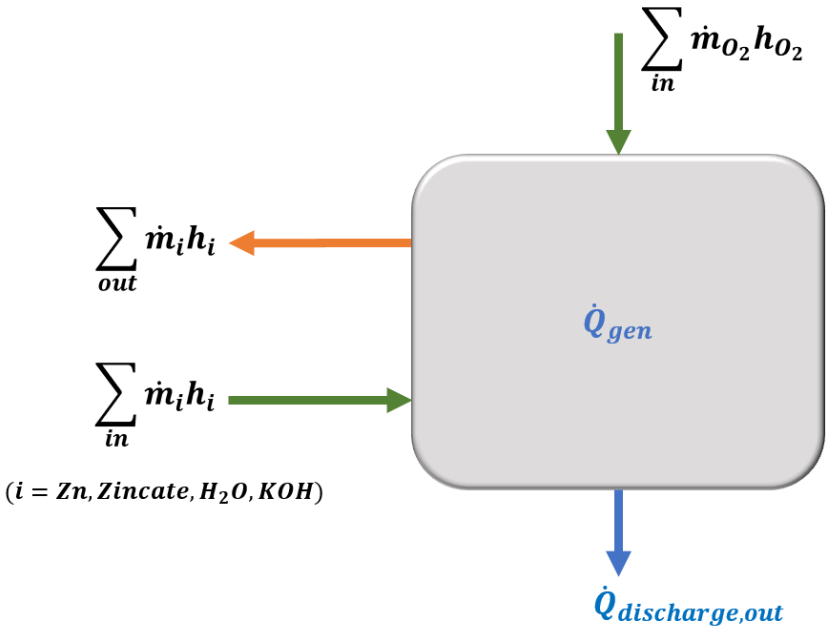

Figure 3.5: Discharge stack heat flows

As shown, heat in the form of enthalpy is transferred into and out of the stack along with the mass flows discussed previously. In addition, there is heat removed from the stack by natural convection, as per the following equation:

$$\dot{Q}_{out} = UA(T - T_{\infty}) \tag{3.7}$$

Where U is the convective heat transfer coefficient, A is the surface area exposed to the convective flow, T is the temperature of the stack, and T_{∞} is the temperature of the environment. The shape of each container was assumed to be a cube, and the cooling area was assumed to be equal to the sum of 4 sides of the cube.

The overall energy balance of the system is derived starting with the 1st law of thermodynamics:

$$\frac{dE}{dt} = \dot{Q} - \dot{W} + \sum_{in} \dot{m}_i h_i - \sum_{out} \dot{m}_i h_i \tag{3.8}$$

where $\frac{dE}{dt}$ is the rate of change of energy in the system, $\dot{Q}$ is the rate of heat transfer, $\dot{W}$ is the rate of work done by the system, and $\sum \dot{m}_i h_i$ is the sum of enthalpy entering and exiting the system for each mass flow of species i. It should be noted that the "system" in this case refers to a single container, specifically the charge or discharge stacks.

The 2nd law of thermodynamics is applied in this case as follows:

$$\frac{dS}{dt} = \frac{\dot{Q}_{in}}{T} + \sum_{in} \dot{n}s - \sum_{out} \dot{n}s + \dot{\Sigma} \tag{3.9}$$

where $\frac{dS}{dt}$ is the rate of change of entropy of the system, $\dot{Q}_{in}$ is the rate of heat entering the system, $\sum \dot{n}s$ is the sum of entropy entering and exiting the system resulting from the molar flows described earlier, and $\dot{\Sigma}$ is the rate of entropy generation. Rearranging yields:

$$T\dot{\Sigma} = T\frac{dS}{dt} - \dot{Q}_{in} - T\sum_{in} \dot{n}s + T\sum_{out} \dot{n}s \tag{3.10}$$

where in the steady state, reversible case:

$$\dot{Q}_{in,rev} = -T\sum_{in} \dot{n}s = T\Delta\dot{S} \tag{3.11}$$

The steady state, irreversible case yields:

$$\dot{\Sigma} = -\frac{\dot{Q}_{in}}{T} - \sum_{in} \dot{n}s = -\frac{\dot{Q}_{in}}{T} + \Delta\dot{S} \tag{3.12}$$

By combining the 1st and 2nd laws:

$$\dot{W} = \dot{W}_{rev} - T\dot{\Sigma} \tag{3.13}$$

where the work loss can be expressed using the difference between the reversible and actual cell potential:

$$T\Sigma = (E_{rev} - E)I \tag{3.14}$$

The internal heat generation can be derived as follows:

$$(E_{rev} - E)I = \eta I = -Q_{in} + T\Delta\dot{S} \tag{3.15}$$

where η is the potential loss of the cell. The rate of entropy generation can be expressed using Faraday's Law of Electrolysis as:

$$\Delta\dot{S} = \Delta s * \frac{I}{nF} \tag{3.16}$$

where Δs is the net standard entropy of the reaction, which for the zinc-air system is:

$$\Delta s = s°[Zn(OH)_4^{2-}] - s°[Zn] - {}^1\!/_2\, s°[O_2] - s°[H_2O] \tag{3.17}$$

The rate of generated heat is therefore:

$$\dot{Q}_{gen} = -\dot{Q}_{in} = \eta I - T\Delta S * \frac{I}{nF} \tag{3.18}$$

The rate of change of energy in the system can then be approximated using the specific heat capacity, mass, and temperature change of the system:

$$mc_p \frac{dT}{dt} = \dot{Q}_{gen} - \dot{Q}_{out} + \sum_{in} \dot{m}_i h_i - \sum_{out} \dot{m}_i h_i \tag{3.19}$$

where m is the mass of the system and c_p is the specific heat capacity of the system. The enthalpy flows can also be expressed using specific heats as well.

$$\sum_{in} \dot{m}_i h_i - \sum_{out} \dot{m}_i h_i = \sum_{in} \dot{m}_i c_{p,i} (T_{in} - T) - \sum_{out} \dot{m}_i c_{p,i} (T_{out} - T) \tag{3.20}$$

Finally, by assuming that the temperature of the outflows from each stack is the same as the stack temperature, the last term drops to zero and the result is:

$$mc_p \frac{dT}{dt} = \dot{Q}_{gen} - \dot{Q}_{out} + \sum_{in} \dot{m}_i c_{p,i} (T_{in} - T) \tag{3.21}$$

The same procedure applies for the charge stack, where the heat flows of the system are shown in Figure 3.6.

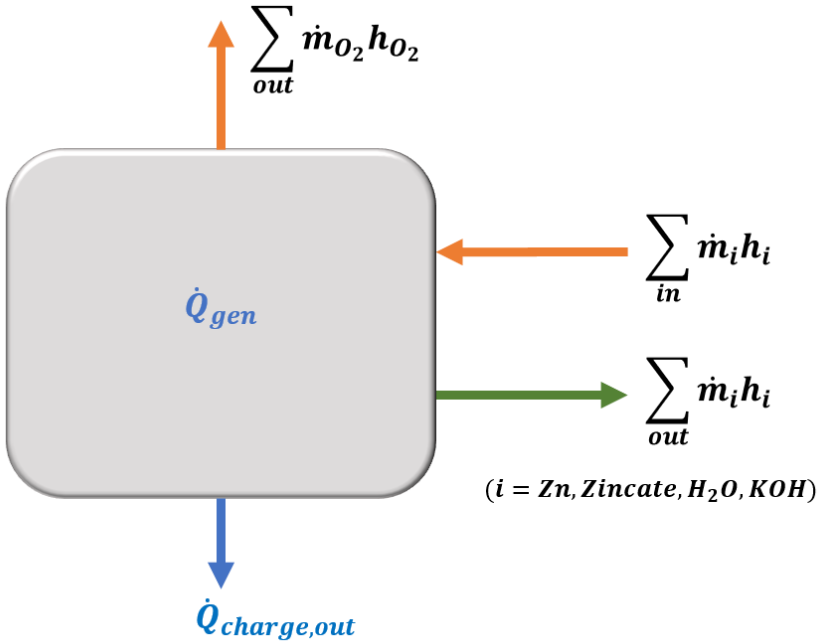

Figure 3.6: Charge stack heat flows

The fuel storage tank is, in comparison, very simple as it is assumed that there are no entropy terms and the flows perfectly mix without any electrochemical activity. The heat flows of the system are shown below in Figure 3.7.

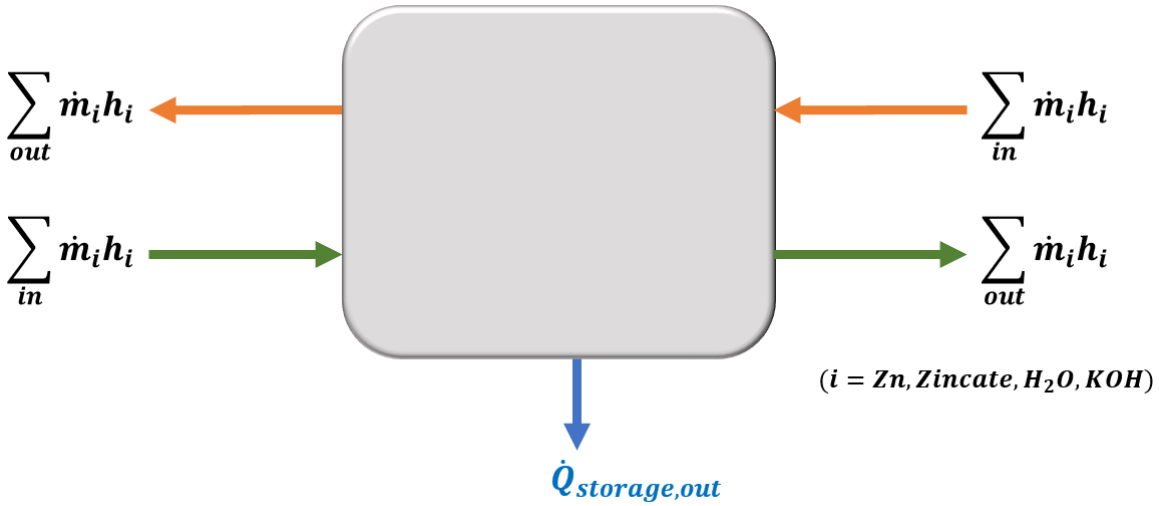

Figure 3.7: Storage tank heat flows

The overall energy balance for the storage tank is therefore:

$$mc_p \frac{dT}{dt} = -\dot{Q}_{out} + \sum_{in} \dot{m}_i c_{p,i} (T_{in} - T) \tag{3.22}$$

3.4 ELECTROCHEMICAL MODEL

The electrochemical model was designed as a zero-dimensional model, where spatial variations are neglected. Other assumptions of the model include:

- Mass transport effects such as diffusion and particle interactions are ignored.
- The concentrations of species at the electrodes, including reactants and products, are assumed to be equal to the concentration of the bulk material in the cell.
- The exchange current densities are assumed to be constant.
- Concentration overpotential is neglected as it typically occurs outside of the range of operation.
- Constant current operation

The state of charge of the system was calculated as follows:

$$SOC = \left(\frac{n_{Zn}}{n_{Zn} + n_{Zincate}}\right)_{storage} \tag{3.23}$$

where the ratio of moles of each species in the storage tank was assumed to be equivalent to that of the entire system. The cell power input/output is described as:

$$P = IE_{cell} \tag{3.24}$$

where P is power and E_{cell} is the cell potential including losses, given by:

$$E_{cell} = E_{cell}^{rev} - \eta_{Ohmic} - \eta_{act}^{Zinc} - \eta_{act}^{air} \tag{3.25}$$

where E_{cell}^{rev} is the reversible cell potential, η_{Ohmic} is the ohmic potential loss, η_{act}^{Zinc} is the activation loss at the zinc electrode, and η_{act}^{air} is the activation loss at the air electrode. The reversible cell potential uses the Nernst equation as follows [5]:

$$E_{cell}^{rev} = \phi^{air} - \phi^{Zinc} \tag{3.26}$$

$$\phi^{air} = E_0^{air} + \frac{RT}{n_e F}\ln\left(\frac{\left(P_{O_2}/P^{ref}\right)^{0.5}}{\left(C_{OH^-}^{air}/C^{ref}\right)^2}\right) \tag{3.27}$$

$$\phi^{Zinc} = E_0^{Zinc} + \frac{RT}{n_e F}\ln\left(\frac{\left(C_{Zn(OH)_4^{2-}}^{Zinc}/C^{ref}\right)}{\left(C_{OH^-}^{Zinc}/C^{ref}\right)^4}\right) \tag{3.28}$$

where E^0 is the standard cell potential, R is the universal gas constant equal to $8.314\frac{J}{molK}$, C_i is the concentration of species i, P_i is the partial pressure of species i, P^{ref} is the reference state pressure of 1 bar, and C^{ref} is the reference state concentration of 1 M. The standard cell potential in this case is given by [5]:

$$E^0 = E^{0,air} - E^{0,zinc} = (0.401\,V) - (-1.199\,V) = 1.6\,V \tag{3.29}$$

The ohmic loss is given by:

$$n_{ohmic} = \frac{I}{A}\frac{L}{\kappa} \tag{3.30}$$

where I is the cell current, A is the cell cross-sectional area parallel to the electrodes, L is the height of the cell, and κ is the electrolyte conductivity, which is calculated using the empirical relation [7] for 45 wt. % potassium hydroxide as follows:

$$\begin{gathered} \kappa(T) = C_1T^3 + C_2T^2 + C_3T + C_4 \\ C_1 = -1.78 * 10^{-7} \\ C_2 = 7.04 * 10^{-5} \\ C_3 = 0.005973 \\ C_4 = 0.270575 \end{gathered} \tag{3.31}$$

where the relation uses T in $°C$ and κ is calculated in S/cm. The activation overpotentials are determined using the Butler-Volmer equation, given by:

$$i = i_0 \cdot \left\{ \exp\left[\frac{\alpha n_e F}{RT}\eta_{act}\right] - \exp\left[-\frac{(1-\alpha)n_e F}{RT}\eta_{act}\right] \right\} \tag{3.32}$$

where i is the current density, α is the charge transfer coefficient which was set to 0.5 for both the zinc and air electrodes [5], i_0 is the exchange current density, and η_{act} is the activation overpotential.

3.5 ALGORITHM

The system starts fully charged at the maximum SOC defined in the user input of the model. Using the user input data, the size of the system is automatically calculated. The process flow diagram of the entire model can be seen below in Figure 3.8. The system then begins the discharge cycle. Once complete,

the system temperatures are reset, and the system is fully charged. Once the full discharge and charge cycles have completed, the energy inputs and outputs of the system are calculated to determine the overall power efficiency. Only one full discharge and charge cycle are performed.

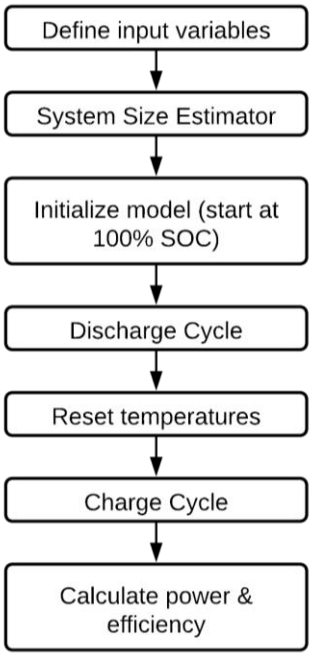

Figure 3.8: Model process flow diagram

The process flow diagram for the discharge cycle is shown below in Figure 3.9. First, the thermodynamically relevant material properties of each species and each tank are calculated.

The charge tank temperature is iteratively solved by making an initial guess, performing the thermal and mass balance, checking whether the newly calculated temperature is within a tolerance limit of the guessed temperature, and iteratively updating the guessed temperature until it is converged. Material is circulated through the charge stack during the discharge cycle in order to distribute equal concentrations of material throughout the system.

The discharge tank follows the same procedure as the charge tank during discharge, with the exception that the cell potential and potential losses are also active and solved iteratively with the thermal balance.

The storage tank follows the same procedure as the charge tank while discharging, with the difference being that material is circulated between both storage tank and both the charge and discharge stacks.

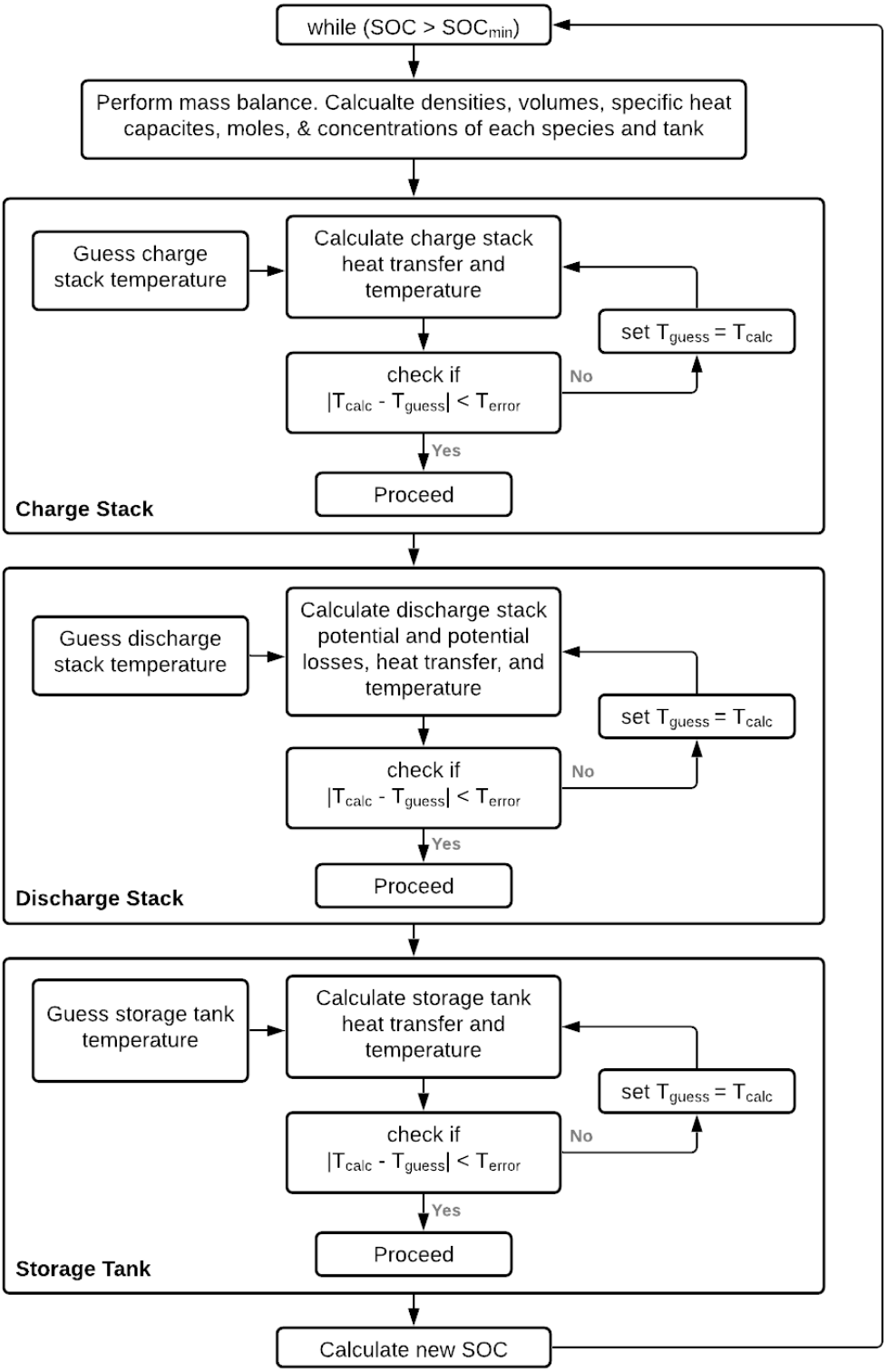

Figure 3.9: Discharge cycle process flow diagram

The charge cycle process flow is the same as the discharge cycle process flow, except that the electrochemical model is added for the charge stack and removed from the discharge stack, and that the while loop condition becomes $while(SOC < SOC_{max})$.

This chapter covered the thermo-electrochemical model that was developed for simulating the specific zinc-air system configuration. The assumptions of the model were outlined, where the objective of the model was to create an order-of-magnitude accurate representation of such a flow battery system. The following chapter will discuss the validation that was performed on the model.

4 MODEL VALIDATION

This chapter will describe results of the model and the validation procedure that was performed.

4.1 VALIDATION APPROACH

Given the novelty of this system's configuration, there were no experimental data from real-world systems with which to compare the theoretical results of this model to. Similarly, nearly all known zinc-air flow battery systems that exist in research create zinc oxide as an end-product rather than zincate. The uniqueness of the chemistry and configuration of this system therefore mandated that the model be validated simply by reviewing the results of the model and analysing the behaviour of the model under certain conditions. Therefore, a reference case was created as a benchmark to evaluate the model performance with system parameters that would be expected in a typical flow battery system.

4.2 REFERENCE CASE INPUT PARAMETERS AND SYSTEM SIZE

The model was validated by simulating a reference case with input values near what would be expected for a typical zinc-air system. Each parameter was evaluated to determine whether it behaved as expected. The reference case was given inputs as shown below in Table 4.1.

Table 4.1: Reference case input parameters

Symbol	Value	Units	Description
E_{rated}	150	*kWh*	Rated capacity
$F_{flow\ rate}$	20	*%*	Flow rate into stack as a percentage of stack volume
$H_{cell,KOH}$	1.0	*mm*	Electrolyte thickness within cell
i	2000	A/m^2	Current density
N_{series}	24	-	Number of cells in series
P_{rated}	20	*kW*	Rated power
SOC_{min}/SOC_{max}	10/95	*%*	Min./Max. SOC
T_0	20	*°C*	Initial system temperature
T_∞	20	*°C*	Ambient temperature
T_{intake}	30	*°C*	Oxygen intake temperature
$U_{natural}$	5	W/m^2K	Overall convection coefficient (natural convection)
$V_{charge,0}$	0.01	m^3	Charge tank volume
$V_{discharge,0}$	0.01	m^3	Discharge tank volume
$V_{storage,0}$	1.00	m^3	Storage tank volume
$X_{KOH,0}$	0.45	*wt. %*	Initial KOH concentration

With the initial conditions described above, the resulting system size was determined as shown in Table 4.2. The discharge and charge stack sizes were equal in this case.

Table 4.2: Reference case system parameters

Symbol	Value	Units	Description
$A_{charge,cell}$	0.011	m^2	Charge cell area
$A_{cooling,storage}$	4.0	m^3	Storage tank cooling area
$A_{discharge,cell}$	0.011	m^2	Discharge cell area
$C_{H_2O,0}$	46.608	*mol/L*	Initial H_2O concentration
$C_{OH,0}$	17.004	*mol/L*	Initial KOH concentration
$C_{Zincate,0}$	0.108	*mol/L*	Initial zincate concentration
$C_{Zn,0}$	2.058	*mol/L*	Initial zinc concentration
I_{charge}	520.8	*A*	Charge stack current
$I_{discharge}$	520.83	*A*	Discharge stack current
$I_{charge,cell}$	21.701	*A*	Charge cell current
$I_{discharge,cell}$	21.701	*A*	Discharge cell current
t_{charge}	6.503	*hours*	Estimated charge time
$t_{discharge}$	6.503	*hours*	Estimated discharge time

4.3 Reference Case Results

The SOC of the system over time can be seen below in Figure 4.1. As shown, the system discharged and immediately afterwards charged to full capacity. The linear change in SOC was expected given the constant current draw and rate of reaction.

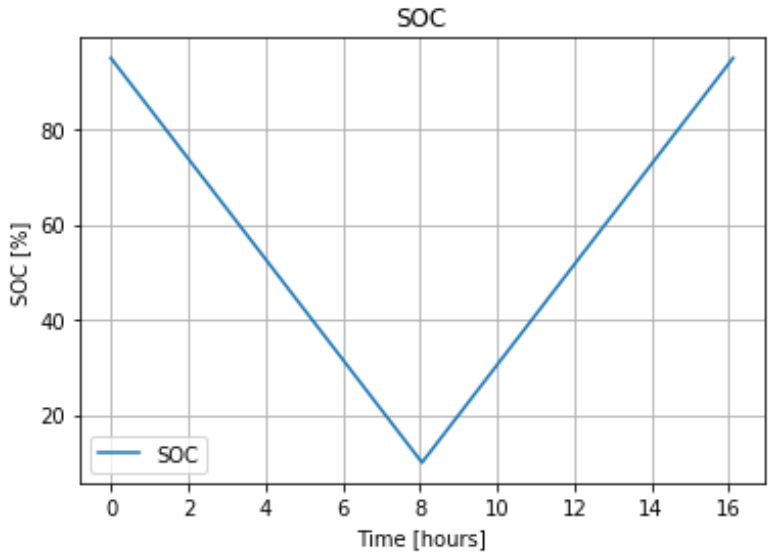

Figure 4.1: Reference case SOC vs. time

Given the overall reaction described in equation (2.3), it is clear to see in Figure 4.2 that the amount of each species changes linearly in proportion to the overall reaction. During discharge, the reactants (H_2O, Zn, and OH^-) all decreased in quantity, while the number of products (zincate) increased. Once discharged, the quantities of each species returned linearly back to the fully charged state as the system is charged.

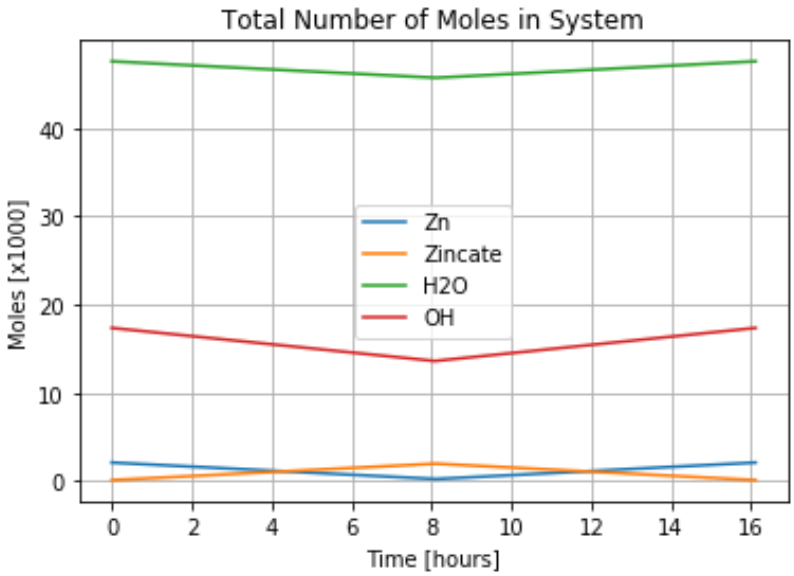

Figure 4.2: Reference case moles vs. time

The conservation of mass for the discharge and charge tanks can be seen clearly in Figure 4.3, where the charge and discharge tanks maintain total masses of 0.022 tonnes, or 22 kg. This small value relative to the storage tank and total mass is explained by the small volume of the stacks defined in the user input. The variation in mass of the storage tank was caused by the addition and removal of oxygen into and out of the system.

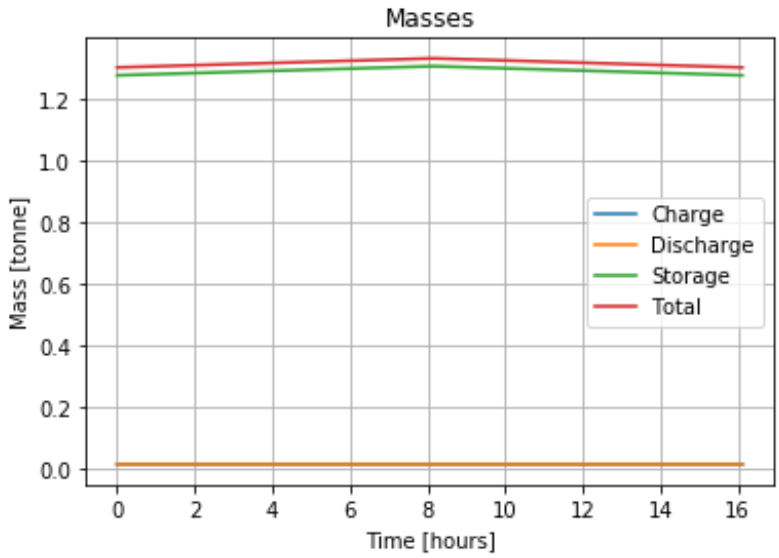

Figure 4.3: Reference case system masses

The system temperatures can be seen below in Figure 4.4. Beginning with the discharge cycle, the system temperatures rise as the reaction proceeds. The charge stack temperature followed the storage tank temperature quite closely during the discharge cycle as there was no electrochemical activity in the charge stack. The discharge stack experienced higher temperatures than the storage tank due to the thermal losses resulting from the electrochemical discharge in the discharge stack. These trends were then maintained throughout discharge.

At the beginning of the charge cycle, the temperatures were manually reset in order to simulate that the system had time to reach its default non-operating temperatures. Once the charge cycle began, the same trend as in the discharge cycle was observed, except that for this case the discharge stack temperature

matched the storage tank temperature, and the charge stack temperature maintained a higher value. The temperature of the charge stack during the charge cycle was slightly less than the temperature of the discharge stack during the discharge cycle because entropy was created during the discharge cycle and absorbed during the charge cycle.

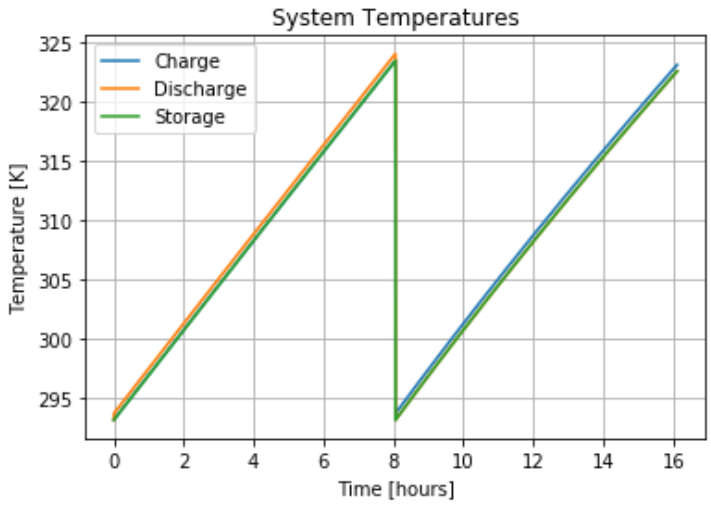

Figure 4.4: Reference case system temperatures

The natural convective cooling can be seen below in Figure 4.5. As shown, the cooling power follows the same trend as the system temperatures, where higher temperatures yield larger cooling rates. Note that the charge and discharge curves overlap.

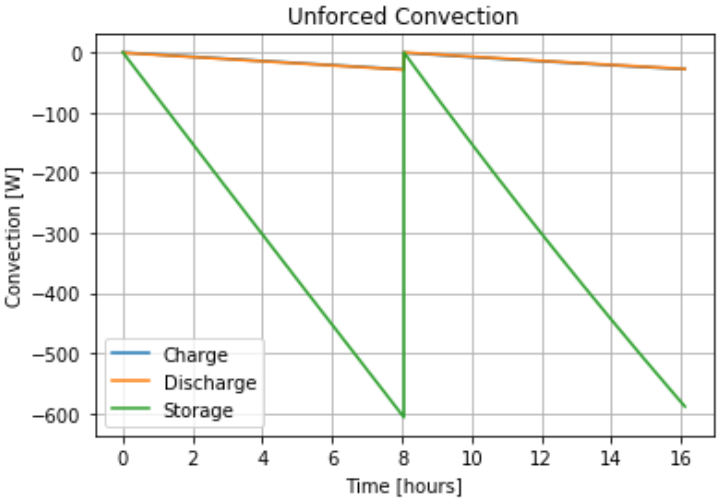

Figure 4.5: Reference case natural convection

The thermal losses from the charge stack while charging and from the discharge stack while discharging can be seen below in Figure 4.6 and Figure 4.7, respectively. As shown, the activation overpotential losses were by far the largest in magnitude, while the ohmic and entropic losses were relatively small (shown by themselves on the right). The changes in magnitude of each curve was due to the temperature changes in the system. Note that the entropic loss was negative for the charge cycle and positive for the discharge cycle.

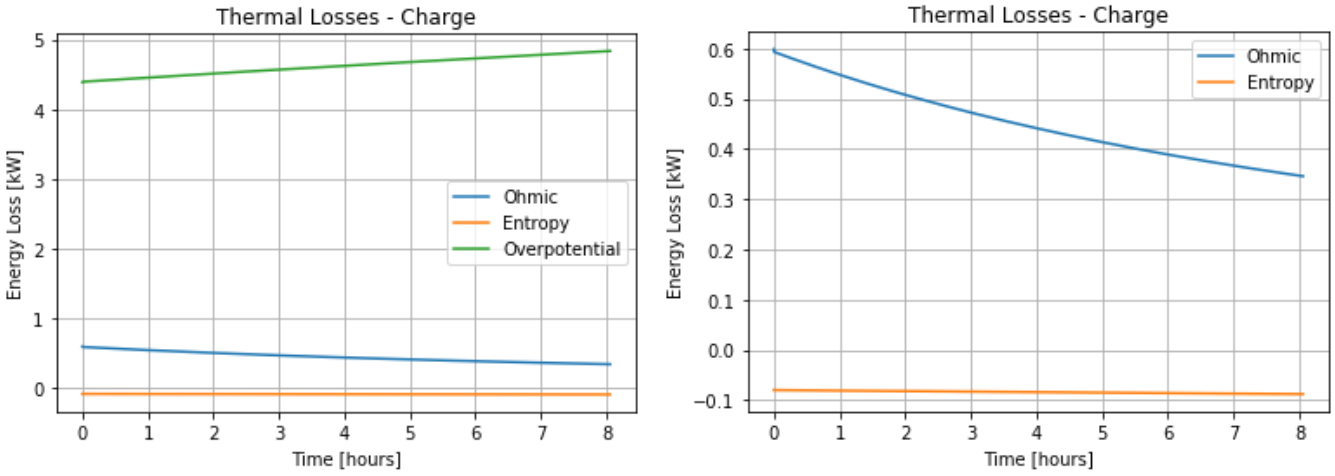

Figure 4.6: Reference case charge stack thermal losses

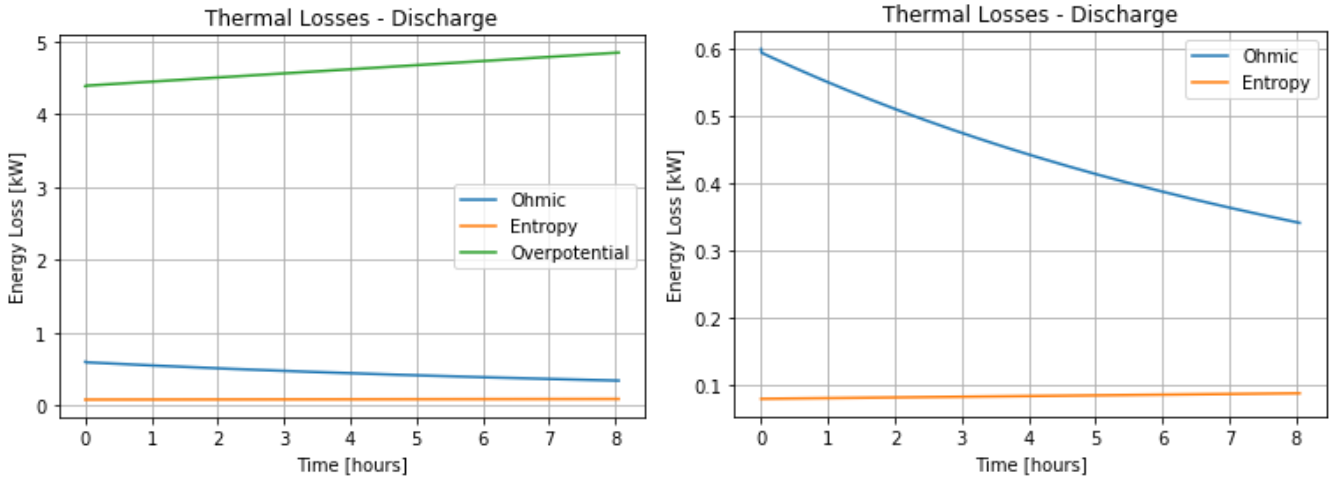

Figure 4.7: Reference case discharge stack thermal losses

The reversible cell potential for charge and discharge can be seen in Figure 4.8. The reversible cell potential is that which comes from the Nernst equation before any losses have been applied. As shown, the potential centers around the standard potential of 1.6 V.

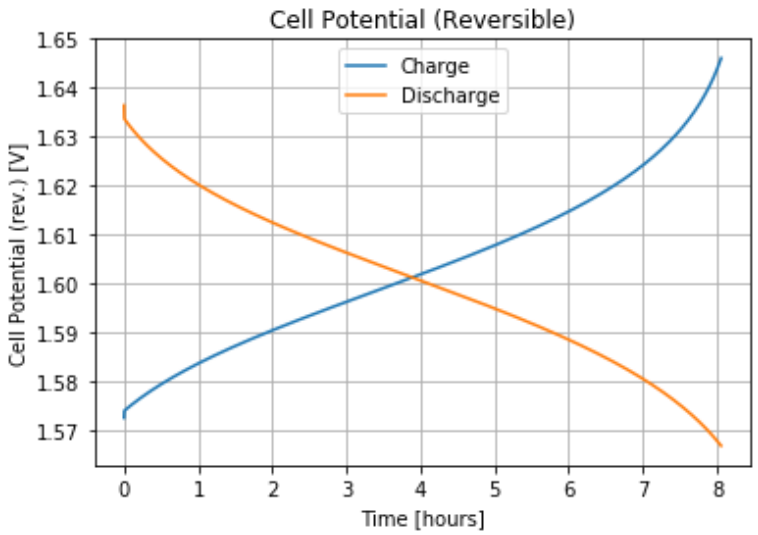

Figure 4.8: Reference case reversible cell potential vs. time

The cell potential with losses included can be seen in Figure 4.9. As shown, there were two main differences between the cell potential and the reversible cell potential. Firstly, the discharge curve was shifted down and the charge curve was shifted up due to the overpotentials. The shape of the curves changed slightly as a result of the changing overpotentials caused by the varying temperatures. The same cell potential is also plotted against SOC as in a typical polarization diagram.

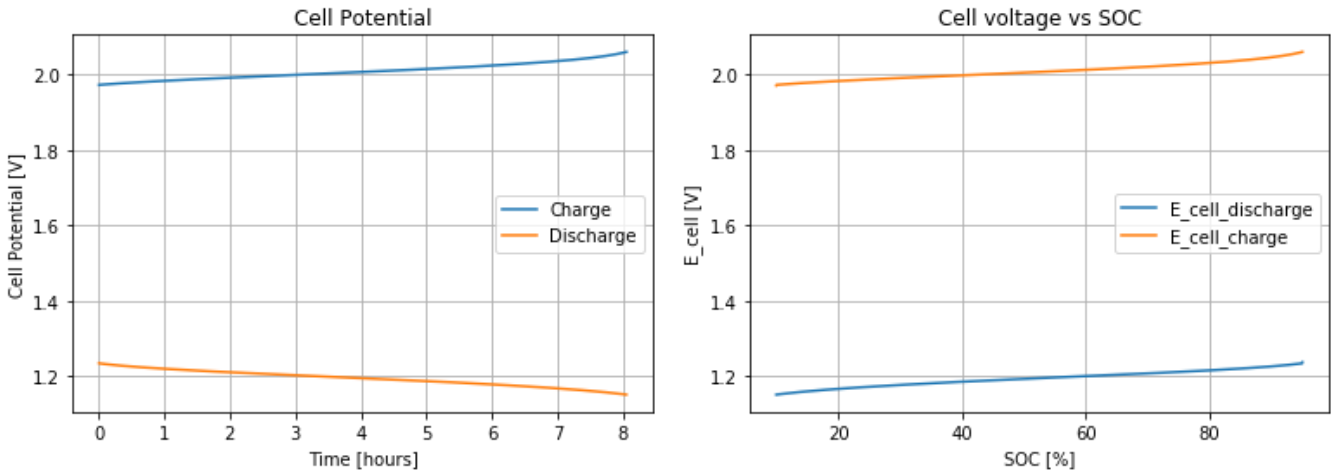

Figure 4.9: Reference case cell potential vs. time/SOC

The overpotentials for the charge and discharge stacks can be seen in Figure 4.10. As shown, the activation overpotentials were by far the largest component of the overpotential losses. With increasing temperature, the activation overpotentials increased, but the ohmic overpotential decreased due to the increase in conductivity with temperature.

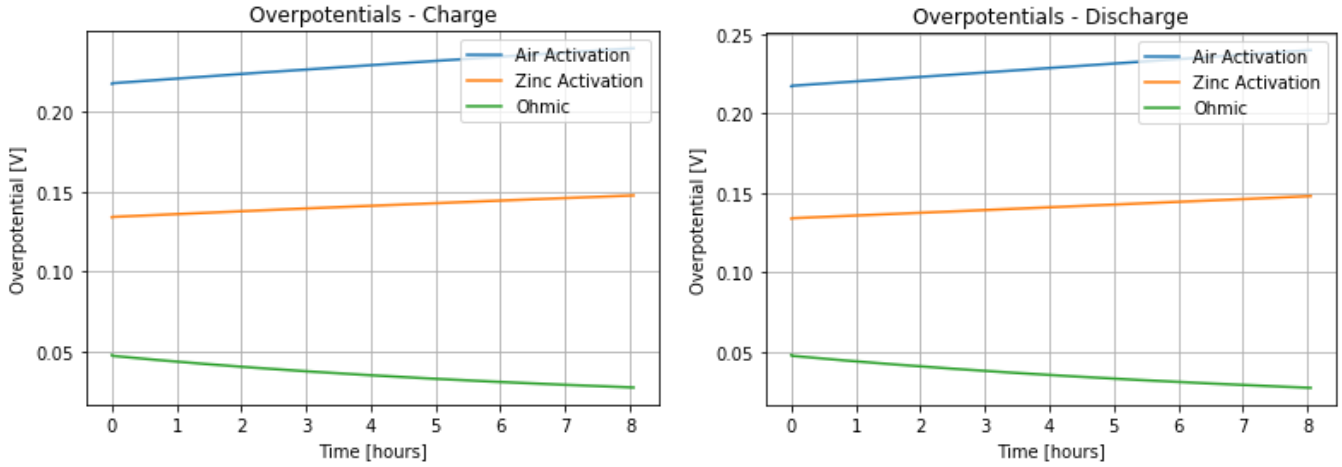

Figure 4.10: Reference case cell overpotentials (charge/discharge)

The electrolyte conductivity can be seen in Figure 4.11, which followed a near-linear trend when plotted against temperature for the operating temperature range.

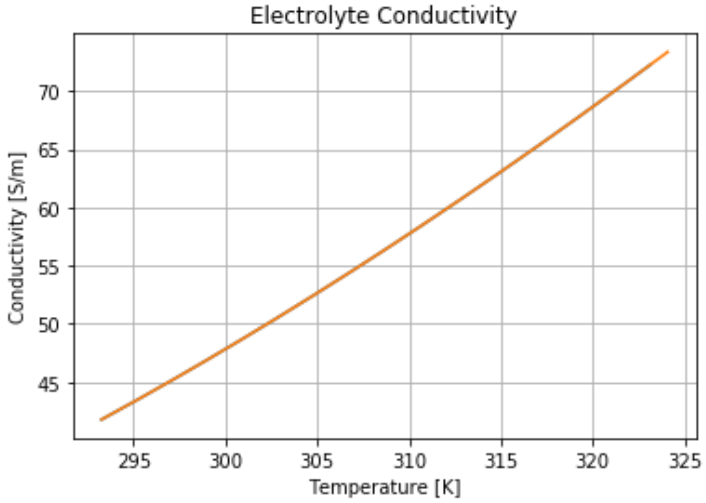

Figure 4.11: Reference case electrolyte conductivity

The resulting energy and efficiency performance of the system can be seen below in Table 4.3.

Table 4.3: Reference case energy and efficiency results

Symbol	Value	Units	Description
E_{in}	202.33	kWh	Energy input to system
E_{out}	120.25	kWh	Energy output from system
$P_{in,avg}$	25.12	kW	Average input power
$P_{out,avg}$	14.93	kW	Average output power
t_{charge}	8.05	$hours$	Total charge time
$t_{discharge}$	8.05	$hours$	Total discharge time
η_{Power}	59.44	$\%$	Power efficiency

4.4 Isothermal Operation Results

To confirm the behaviour of the electrochemical model, the temperature was forced to be constant by making the natural convection coefficient very large, which would force any increase in temperature

above ambient to be immediately cooled back to ambient temperature. The cell potentials can be seen below in Figure 4.12, where very similar results were obtained as in the reference case.

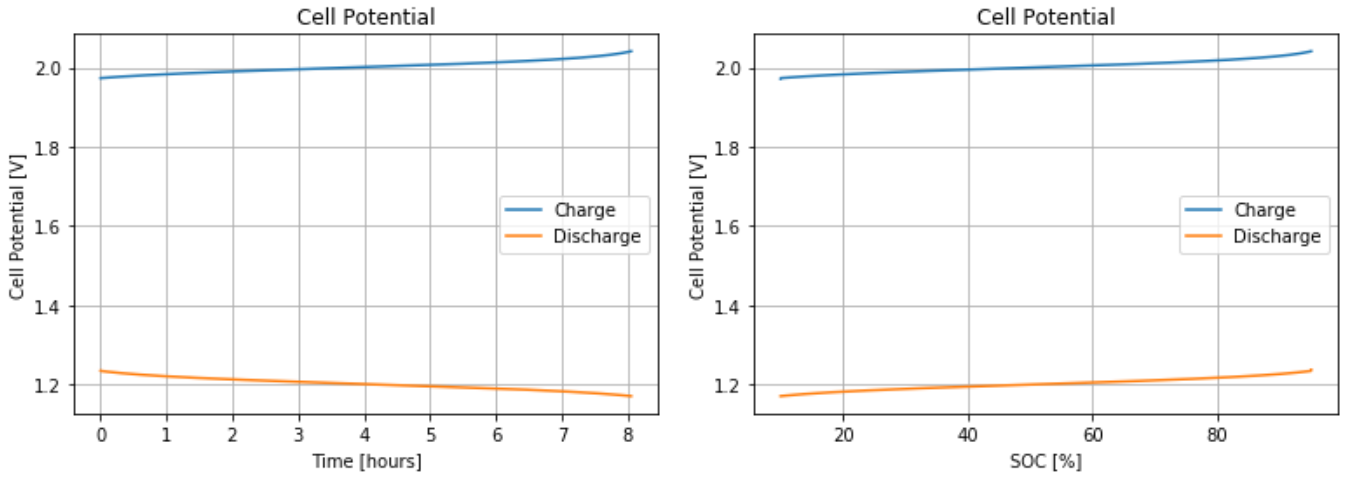

Figure 4.12: Isothermal case cell potential

The overpotentials can be seen below in Figure 4.13. In this case, the overpotentials remained constant because of the constant temperature. Similarly, the thermal losses also remained constant, shown below in Figure 4.14.

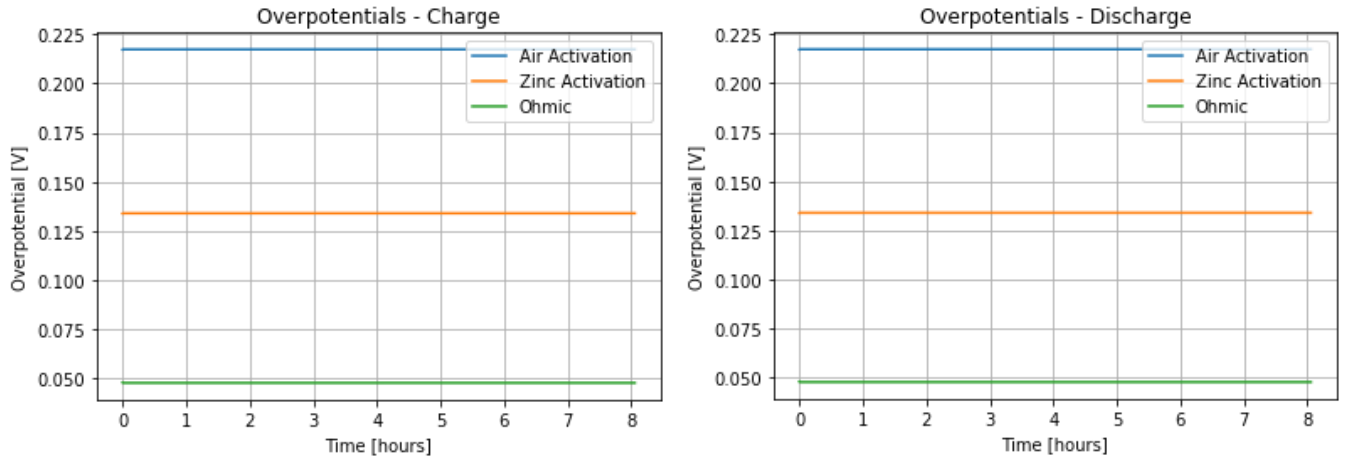

Figure 4.13: Isothermal case cell overpotentials

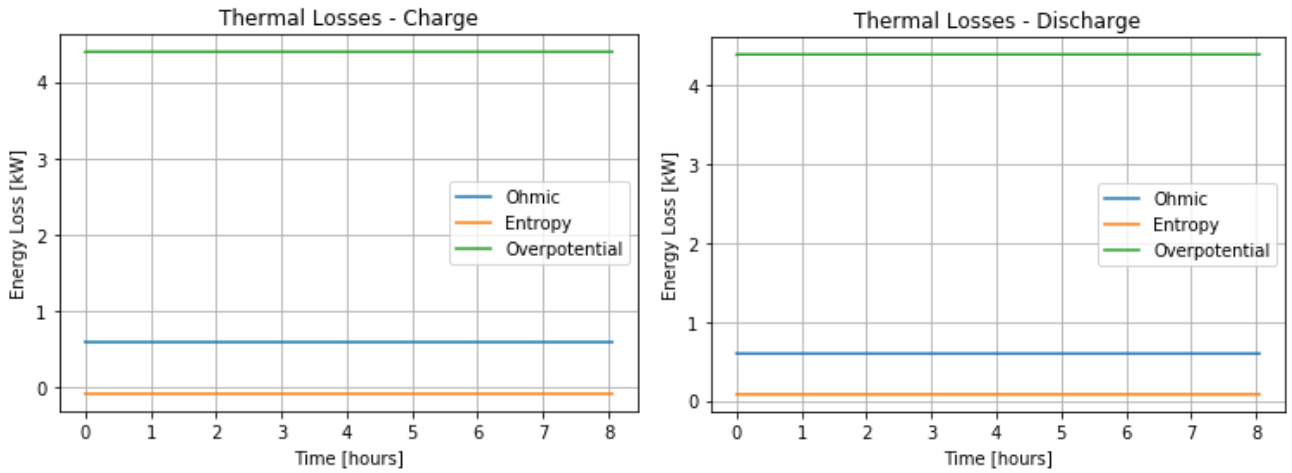

Figure 4.14: Isothermal case stack thermal losses

The natural convective cooling which counteracted the thermal losses to maintain constant temperature can be seen below in Figure 4.15.

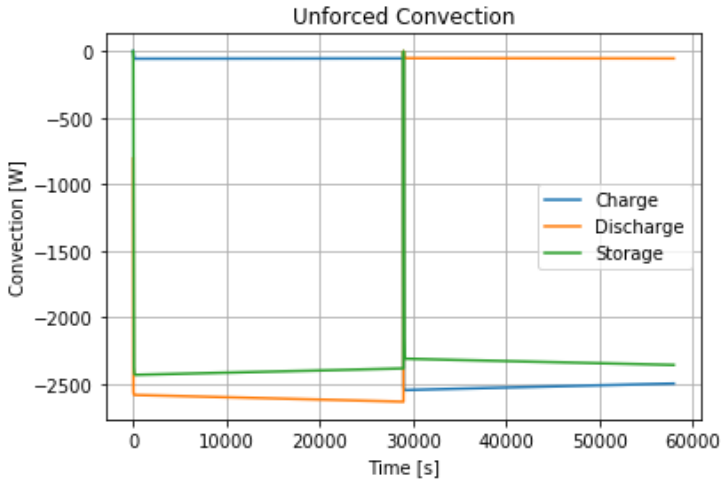

Figure 4.15: Isothermal case natural convection

Lastly, the energy and efficiency results are given in Table 4.4. The performance parameters of the system changed by a very small amount, in keeping with the small changes in cell potential.

Table 4.4: Isothermal case energy and efficiency results

Symbol	Value	Units	Description
E_{in}	201.59	kWh	Energy input to system
E_{out}	120.99	kWh	Energy output from system
$P_{in,avg}$	25.03	kW	Average input power
$P_{out,avg}$	15.02	kW	Average output power
t_{charge}	8.05	*hours*	Total charge time
$t_{discharge}$	8.05	*hours*	Total discharge time
η_{Power}	60.02	%	Power efficiency

4.5 DISCUSSION OF VALIDATION RESULTS

The mass balance and thermal balance of the model performed as expected given the model input parameters. The flows of material were seen to change as expected. The system temperatures varied as expected and mass was conserved throughout the system, with constant mass observed in the charge and discharge stacks.

To validate the electrochemical model, the results were compared with similar results from Lao-atiman et al [5]. The electrochemical model resembled the results of Lao-atiman et al. as expected, though the reversible cell voltage did not vary with SOC as it should have. The Nernst equation used the concentration of zincate and zinc as the reductant and oxidant, respectively. This was an approximation that was made in place of using water, hydroxyl, and zinc as the oxidants because the latter approach resulted in reversible cell potentials that were too high, centering around approximately 1.8 V rather than 1.6 V. The activation overpotentials were of approximately the expected magnitude, but they were likely quite inaccurate as the exchange current density was fixed at one value. Multiple expressions for activation

overpotential were investigated, but most expressions relied on detailed knowledge of the mass transport behaviour within the cell, which this model ignored. In the case of both activation overpotentials, the formulas found for exchange current density that were obtained from literature were found to yield unreasonable values. Therefore, the exchange current densities were set as fixed using values taken from literature of an appropriate order of magnitude. In the case of the zinc activation overpotential, even the exchange current density values that were found also varied by multiple orders of magnitude, so a value that yielded approximately reasonable results was chosen from the literature [6].

Overall, the model was found to perform well for an order-of-magnitude level of accuracy. In the absence of mass transport modelling for the electrochemical model, the activation overpotentials of the system were likely quite inaccurate though they produced results of the expected order of magnitude. The system efficiency is likely overestimated as other effects such as pump losses were not included.

This chapter detailed the validation of the model against a reference case and an isothermal case where the simulation outputs were compared with [5] where possible. The following chapter will discuss two case studies that were completed to gain insight into the performance of the zinc-air flow battery in the novel configuration.

5 CASE STUDIES

The following section outlines two different case studies to evaluate the thermal response of the system to changes in rated power and flow rate.

5.1 CASE I: POWER RESPONSE

To evaluate the response of the system to differences in rated power, the performance was simulated for rated powers from 10 to 30 kW and the thermal and electrical responses were observed. The system parameters were kept the same as in the reference case, with rated power being the only parameter which was changed. However, the rated power greatly affects the cell size and current (ideal voltage of 1.6 V assumed when calculating system size). The resulting system parameters that differed due to the change in rated power can be seen below in Table 5.1.

Table 5.1: Case I system parameters

Power	**10**	**15**	**20**	**25**	**30**	**kW**
$A_{charge,cell}$	0.005	0.008	0.011	0.014	0.016	m^2
$A_{discharge,cell}$	0.005	0.008	0.011	0.014	0.016	m^2
I_{charge}	260.42	390.63	520.83	651.04	781.25	*A*
$I_{discharge}$	260.42	390.63	520.83	651.04	781.25	*A*
$I_{charge,cell}$	10.851	16.276	21.701	27.127	32.552	*A*
$I_{discharge,cell}$	10.851	16.276	21.701	27.127	32.552	*A*
t_{charge}	13.005	8.670	6.503	5.202	4.335	*hours*
$t_{discharge}$	13.005	8.670	6.503	5.202	4.335	*hours*

The temperature development of the storage tank with varying rated power can be seen below in Figure 5.1 for the charge and discharge cycles. As shown, the temperature increased in the storage tank

more quickly as the power increased. Similarly, the total time required to discharge decreased with increasing power. Similar trends were observed for both charge and discharge.

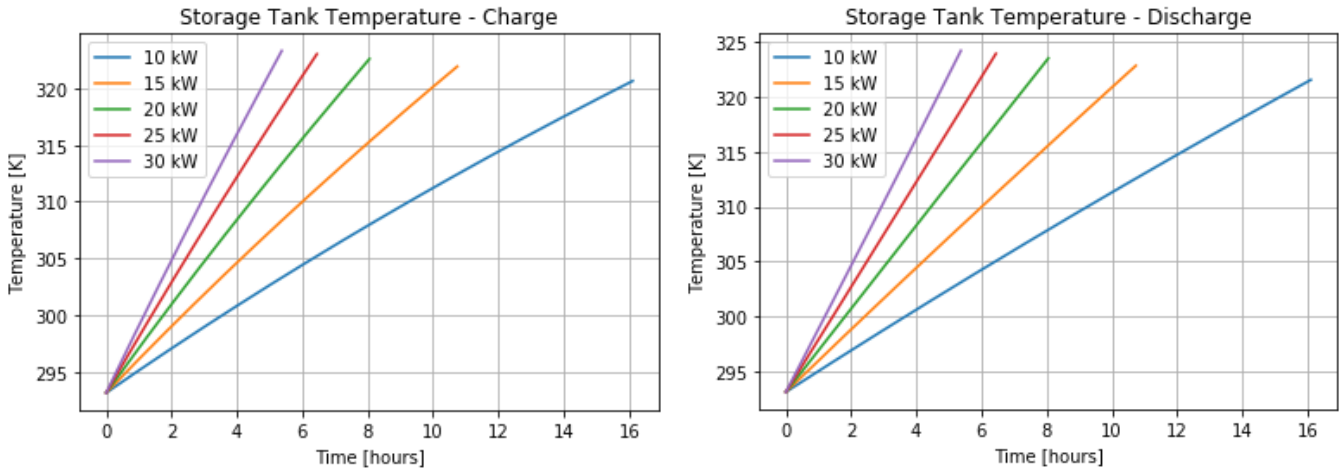

Figure 5.1: Case I storage tank temperatures

The maximum temperatures throughout the simulation can be seen below in Figure 5.2. As shown, the maximum temperature observed in the system increased with increasing rated power. The discharge stack maintained a higher temperature than the storage tank because entropy increased the system temperature during the discharge reaction. The charge stack temperatures were quite close to the storage tank temperatures because the entropy was consumed in the charge reaction, thus slightly lowering the temperature (the charge stack temperature is shown in the plot as overlapping with the storage tank temperature). The difference between the storage tank and discharge stack temperatures increased with increasing power because the volume of the stacks was constant at 0.01 m^3 for all rated powers while the current and therefore generated heat increased.

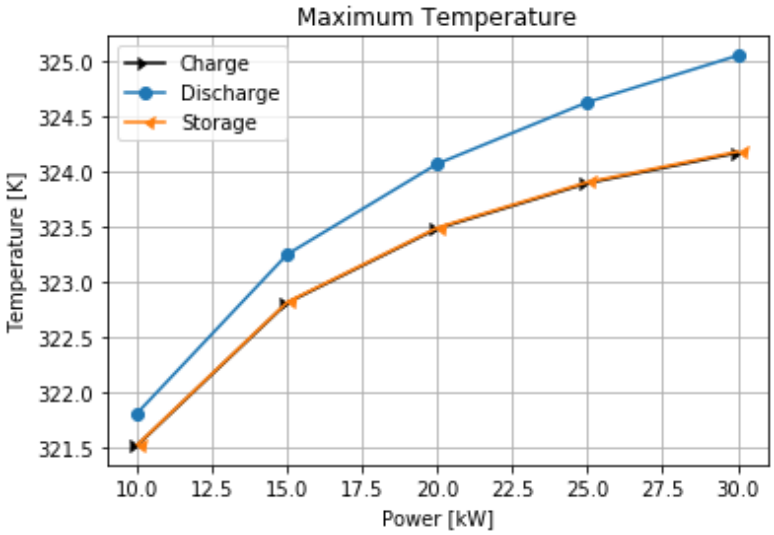

Figure 5.2: Case I maximum temperatures

The overpotentials of the system at various rated powers are shown below in Figure 5.3. For both the activation overpotentials, higher power yielded higher overpotential losses. The opposite trend was observed for the ohmic overpotentials, where higher power yielded lower ohmic potentials, likely due to the increase in temperature of the system.

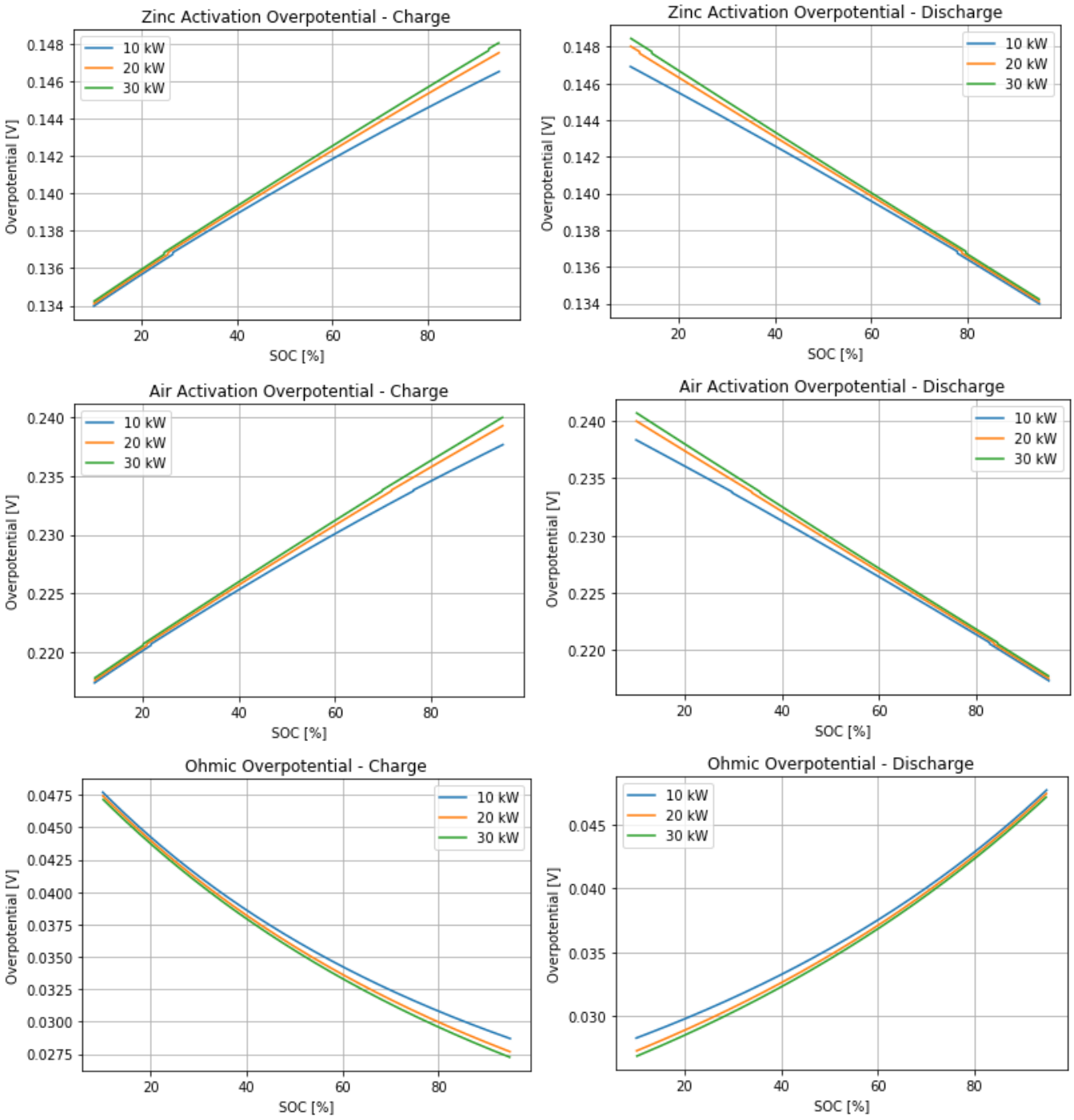

Figure 5.3: Case I overpotentials

The cell potentials for various rated powers is shown in Figure 5.4. Nearly identical values were found for each case, and in practise the rated power did not affect the potential significantly. That said, the

increase in power made the charge cell potential slightly higher and the discharge cell potential slightly lower, in keeping with the increase in overpotential with increasing power.

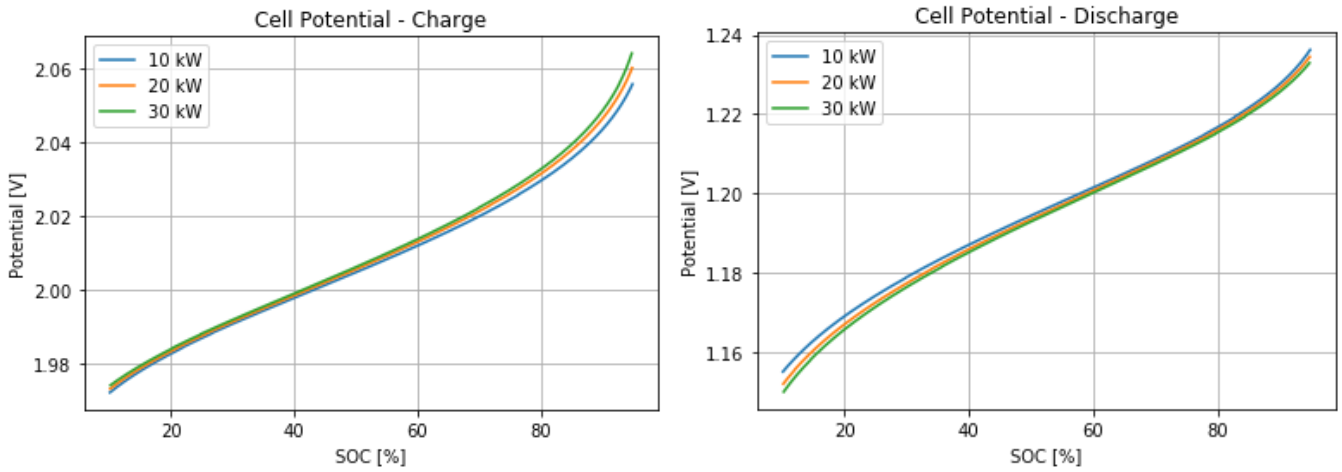

Figure 5.4: Case I cell potentials

5.2 Case II: Flow Rate Response

The temperature response of the system to varying flow rate was also simulated. The flow rate was defined as a fraction of the charge stack volume, where a flow rate factor of 20 % would mean that 20 % of the volume of the stack would be recirculated each second. All input parameters excluding the flow rate factor were defined using values from the reference case. The flow rate factor was varied between 5 % and 50 %. Values below 5 % were not possible because it would not provide enough circulation of the fluid to replenish the zinc supply given the reaction rate. The flow rates in *L/s* are shown below in Table 5.2 with their corresponding flow rate factors.

Table 5.2: Case II flow rates

Flow Rate Factor (%)	**Flow Rate (*L/s*)**
5	0.5
10	1.0
20	2.0
30	3.0
40	4.0
50	5.0

The storage tank temperatures at different flow rates can be seen below in Figure 5.5. As shown, the temperature of each flow rate directly overlaps on one another, and therefore no noticeable differences in the overall temperature development of the storage tank was observed.

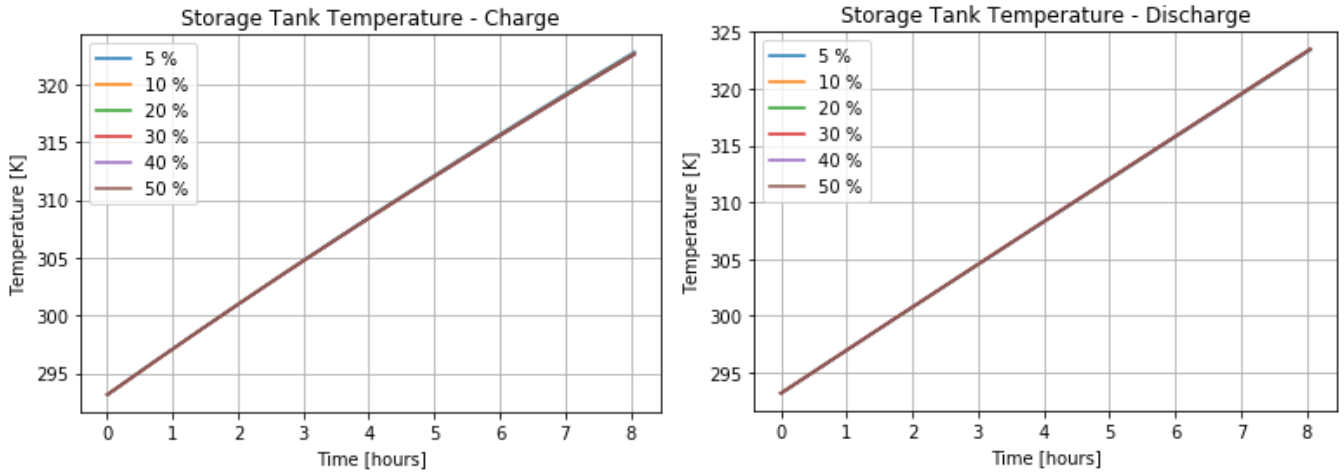

Figure 5.5: Case II storage tank temperatures

The change in maximum temperature throughout charge and discharge with flow rate can be seen below in Figure 5.6. As shown, there is a change on the order of 2 degrees in temperature among the flow rate factors that were simulated. For both the charge and discharge stacks, the temperature increased with

decreasing flow rate as expected. As flow rate increased, the temperatures of each part of the system approached the same value. The storage tank temperature increased with increasing flow rate factor due to the addition of more heat being transferred into the storage tank from the stacks.

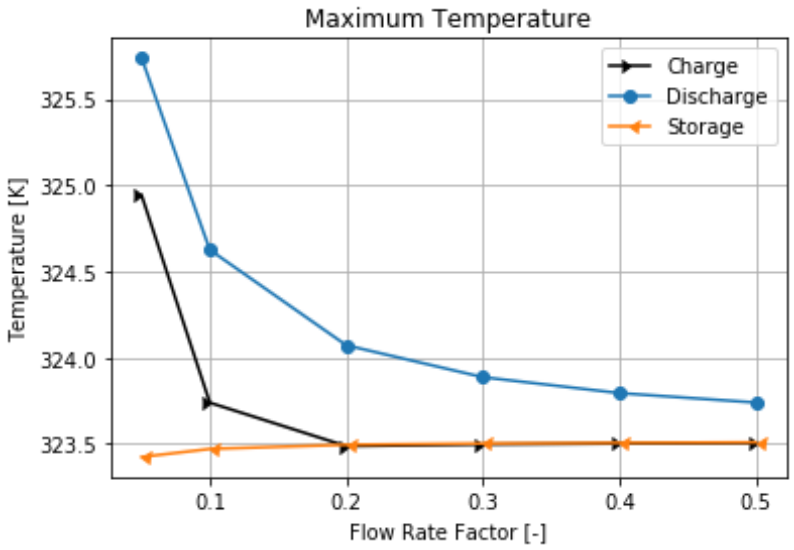

Figure 5.6: Case II maximum temperatures

The change in overpotentials with flow rate can be seen below in Figure 5.7. Similar trends as for the first case study were observed, where with decreasing flow rate, the stack temperatures increased. This increase in stack temperature increased the activation overpotentials while decreasing the ohmic overpotential.

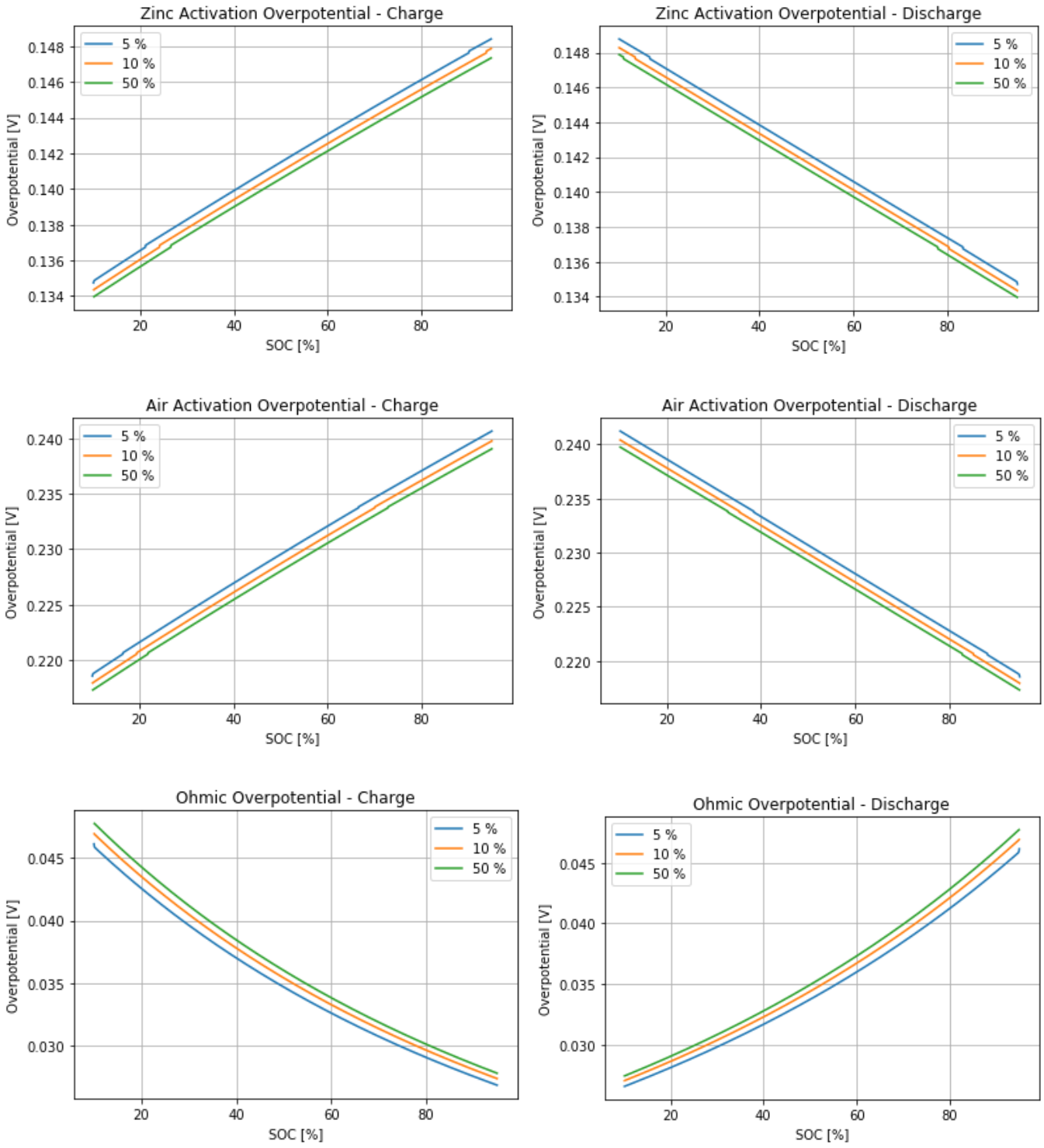

Figure 5.7: Case II overpotentials

Lastly, the cell potentials at varying flow rates can be seen bellow in Figure 5.8. As expected, the charge cell potential increased with decreasing flow rate and the discharge cell potential decreased with decreasing flow rate. One interesting behaviour was the high spike in the charge cell potential at 5 % flow rate factor. This was caused by the reversible cell potential, where the low concentration of zincate caused the cell potential to drastically increase due to the logarithmic behaviour.

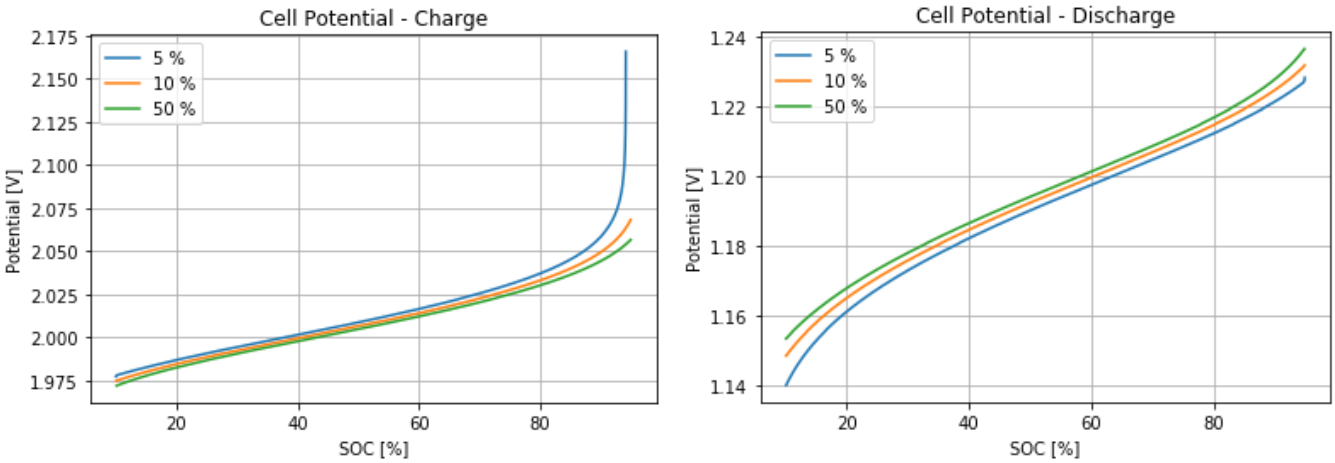

Figure 5.8: Case II cell potentials

5.3 Discussion of Case Study Results

The behaviour of the system in response to the two case studies that were performed was in keeping with the expected results from such a system. In terms of practical design, the power of the cell is largely determined by the load requirements of a particular site or application. Therefore, there is often little room for negotiation when it comes to choosing the rated power of the system. That said, the change in temperature that was observed as a result of changing the rated power is of particular note to designers, where materials must be selected to withstand certain operating conditions, among other design factors.

In regards to flow rate, the largest concern was to select a flow rate that ensures there is sufficient zinc in the discharge stack (or similarly, that there is enough zincate in the charge stack) in order for the electrochemical processes to be carried out effectively. Beyond that, the flow rate could also be dynamically controlled to adjust the temperature of the containers relative to each other in the case that the stacks may have an ideal operating temperature that would differ from the ideal storage tank temperature.

This chapter discussed two case studies that were used to further evaluate the model and test the response of the system to different design parameters. The following chapter will summarize the work that was performed in developing the model, the validation process, and case studies, and give some recommendations for how the model could be improved in the future.

6 CONCLUSION

This chapter will summarize the results of the model development and discuss future improvements that can be made to the model.

6.1 SUMMARY

A thermo-electrochemical model was developed with the intention to assist academia and industry in the development of new zinc-air flow battery systems. A novel approach was simulated which featured independent charging and discharging stacks connected via a large fuel storage reservoir. The decoupling of these three systems enables independent scaling of discharge power, input power, and capacity. Secondly, the model also produces zincate as an end-product where most systems that exist in the literature produce zinc oxide [5]. The model was successfully developed and validated to be suitable for order-of-magnitude accurate approximations to system performance and size. As research continues into large grid energy storage systems, more attention will be paid to innovative solutions, particularly in the field of zinc-air flow batteries.

The model was validated by comparing the results of a reference case and an isothermal case to the performance of the model developed by Lao-atiman et al [5]. The model was found to produce reasonable results within an order of magnitude and was able to demonstrate trends in thermal and electrochemical responses to changes in design parameters. A rated power case study and a flow rate case study were performed and discussed.

6.2 RECOMMENDATIONS FOR FUTURE WORK

To further develop the model while improving its accuracy, the inclusion of a more detailed electrochemical model would enable more realistic activation overpotentials to be obtained. By including mass transport and diffusion effects, more sophisticated relationships could be obtained. Secondly, the

model could be improved by providing more detail to the thermal model such as housing geometry, conductive heat loss, pumps with their related thermal effects, and capturing the energy expended to actively cool the storage tank in the overall thermal balance. It would also be recommended to move the model from Jupyter Notebooks where it was developed into a standalone python program running in a dedicated development environment to improve the reliability of the model execution.

7 REFERENCES

[1] R. K. Sen, S. L. Van Voorhees and T. Ferrel, "Metal-Air Battery Assessment," Battelle, 1988.

[2] M. A. Rahman, X. Wang and C. Wen, "A review of high energy density lithium-air battery technology," *Journal of Applied Electrochemistry,* vol. 44, pp. 5-22, 2014.

[3] P. C. Foller, "Improved slurry zinc/air systems as batteries for urban vehicle propulsion," *Journal of Applied Electrochemistry,* vol. 16, pp. 527-543, 1986.

[4] J. Fu, Z. P. Cano, M. G. Park, A. Yu, M. Fowler and Z. Chen, "Electrically Rechargeable Zinc-Air Batteries: Progress, Challenges, and Perspectives," *Advanced Materials,* vol. 29, pp. 1-34, 2017.

[5] W. Lao-atiman, K. Bumroongsil, A. Arpornwichanop, P. Bumroongsakulsawat, S. Olaru and S. Kheawhom, "Model-Based Analysis of an Integrated Zinc-Air Flow Battery/Zinc Electrolyzer System," *Frontiers in Energy Reserach,* vol. 7, pp. 1-15, 2019.

[6] A. R. Despic, D. Jovanovic and T. Rakic, "Kinetics and Mechanism of Deposition of Zinc from Zincate in Concentrated Alkali Hydroxide Solutions," *Electrochemica Acta,* vol. 21, pp. 63-77, 1976.

[7] F. Allebrod, P. L. Mollerup, C. Chatzichristodoulou and M. B. Mogensen, "Electrical conductivity measurements of aqueous and immobilized potassium hydroxide," in *DTU Library*, 2011.

[8] National Institute of Standards and Technology, "Zinc," U.S. Department of Commerce, 2018. [Online]. Available: https://webbook.nist.gov/cgi/inchi/InChI%3D1S/Zn. [Accessed 18 November 2020].

[9] National Institute of Standards and Technology, "Zinc Oxide," U.S. Department of Commerce, 2018. [Online]. Available: https://webbook.nist.gov/cgi/formula?ID=C1314132. [Accessed 18 November 2020].

[10] National Institute of Standards and Technology, "Water," U.S. Department of Commerce, 2018. [Online]. Available: https://webbook.nist.gov/cgi/cbook.cgi?ID=C7732185. [Accessed 18 November 2020].

[11] National Institute of Standards and Technology, "Potassium Hydroxide," U.S. Department of Commerce, 2018. [Online]. Available: https://webbook.nist.gov/cgi/cbook.cgi?ID=C1310583&Mask=2. [Accessed 18 November 2020].

[12] T. P. Dirkse and H. N. A., "The Zn(II)/Zn Exchange Reaction in KOH Solutoin - III. Exchange Current Measurements Using the Potentiostatic Method," *Electrochimica Acta,* vol. 17, pp. 1113-1119, 1972.

[13] X. Song, J. Zhang, J. Fu, H. Zarrin, X. Tian, J. Qiao, L. Rasen, K. Li and Z. Chen, "A flexible solid-state electrolyte for wide-scale integration of rechargeable zinc-air batteries," *Energy & Environmental Science,* vol. 9, no. 2, pp. 663-670, 2016.

[14] Wikipedia, "Faraday Constant," Wikipedia, 6 November 2020. [Online]. Available: https://en.wikipedia.org/wiki/Faraday_constant. [Accessed 18 November 2020].

[15] E. Potvin and L. Brossard, "Electrocatalytic activity of Ni-Fe anodes for alkaline water elctrolysis," *Materials Cheimstry and Physics,* vol. 31, no. 4, pp. 311-318, 1992.

[16] L. An, T. S. Zhao, Z. H. Chai and L. Zeng, "Mathematical modeling of an anion-exchange membrane water electrolyzer for hydrogen production," *International Journal of Hydrogen Energy,* vol. 39, pp. 19869-19876, 2014.

[17] Endmemo, "Zincate Ion," Endmemo, 2020. [Online]. Available: http://www.endmemo.com/chem/compound/znoh_4.php. [Accessed 18 November 2020].

[18] National Institute of Standards and Technology, "Potassium hydroxide," U.S. Department of Commerce, 2018. [Online]. Available: https://webbook.nist.gov/cgi/cbook.cgi?ID=1310-58-3&Units=SI. [Accessed 20 November 2020].

[19] National Institute of Standards and Technology, "Hydroxyl anion," U.S. Department of Commerce, 2018. [Online]. Available: https://webbook.nist.gov/cgi/cbook.cgi?ID=C14280309&Mask=1000. [Accessed 18 November 2020].

[20] National Institute of Standards and Technology, "Oxygen," U.S. Department of Commerce, 2018. [Online]. Available: https://webbook.nist.gov/cgi/cbook.cgi?ID=7782-44-7. [Accessed 18 November 2020].

[21] Wikipedia, "Gas constant," Wikipedia, 10 November 2020. [Online]. Available: https://en.wikipedia.org/wiki/Gas_constant. [Accessed 18 November 2020].

[22] Z. Mao and R. E. White, "Mathematical Modeling of a Primary Zinc/Air Battery," *Journal of the Electrochemical Society,* vol. 139, pp. 1105-1114, 1992.

[23] J. Pan, Y. Y. Xu, H. Yang, Z. Dong, H. Liu and B. Y. Xia, "Advanced Architectures and Relatives of Air Electrodes in Zn-Air Batteries," *Advanced Science,* vol. 5, pp. 1-30, 2018.

[24] L. M. Ibarra, *Thermoelectrochemical model for RFB with application at a grid level for peak shaving to reduce the cost of the total electricity,* 2020.

[25] L. Reining, M. Bockelmann, U. Kunz and T. Turek, "Kinetics of active zinc dissolution in concentrated KOH solutions," *Journal of Applied Electrochemistry,* vol. 50, pp. 149-158, 2020.

[26] A. R. Mainar, O. Leonet, M. Bengoechea, I. Boyano, I. d. Meatza, A. Kvasha, A. Guerfi and J. A. Blazquez, "Alkaline aqueous electrolytes for secondary zinc-air batteries: an overview," *International Journal of Energy Research,* vol. 40, pp. 1032-1049, 2016.

APPENDIX I: MODEL PARAMETERS

Symbol	Value	Unit	Description	Source
$c_{p,Zn}$	25.47	*J/molK*	Specific heat of zinc	[8]
$c_{p,Zincate}$	40.3	*J/molK*	Specific heat of zincate	[9]*
c_{p,H_2O}	75.23	*J/molK*	Specific heat of H_2O	[10]
c_{p,OH^-}	65.87	*J/molK*	Specific heat of OH	[11]**
E_0^{zinc}	-1.199	*V*	Standard zinc electrode potential	[12]
E_0^{air}	0.401	*V*	Standard air electrode potential	[13]
F	96,485	*C/mol*	Faraday's constant	[14]
i_0^{air}	0.37	*A/m²*	Exchange current density of air electrode	[15, 16]
i_0^{zinc}	10	*A/m²*	Exchange current density of zinc electrode	[6]
M_{Zn}	65.38	*g/mol*	Molar mass of zinc	[8]
$M_{Zincate}$	133.41	*g/mol*	Molar mass of zincate	[17]
M_{H_2O}	18.02	*g/mol*	Molar mass of H_2O	[10]
M_{KOH}	56.11	*g/mol*	Molar mass of KOH	[18]
M_{OH^-}	17.01	*g/mol*	Molar mass of OH^-	[19]
M_{O_2}	32.00	*g/mol*	Molar mass of O_2	[20]
n_e	2	-	Electrons transferred per reaction	[5]
R	8.314	*J/molK*	Universal gas constant	[21]
$s°[Zn]$	41.72	*J/molK*	Standard specific entropy of zinc	[8]
$s°[ZnO]$	43.7	*J/molK*	Standard specific entropy of zinc oxide	[9]
$s°[O_2]$	205.15	*J/molK*	Standard specific entropy of oxygen	[20]
α_{zinc}	0.5	-	Zinc charge transfer coefficient	[5]
α_{air}	0.5	-	Air charge transfer coefficient	[5]
ρ_{Zn}	7140	*kg/m³*	Density of zinc	[8]
$\rho_{Zincate}$	5610	*kg/m³*	Density of zincate	[9]*
ρ_{H_2O}	997	*kg/m³*	Density of H_2O	[10]
ρ_{OH^-}	2120	*kg/m³*	Density of KOH	[11]**
ρ_{KOH}	2120	*kg/m³*	Density of KOH	[11]

* using value for ZnO in absence of zincate data

** using value of KOH in absence of hydroxyl ion data